HHS Public Access

Author manuscript

Neuron. Author manuscript; available in PMC 2021 March 02.

Published in final edited form as:

Neuron. 2020 July 08; 107(1): 65–81.e9. doi:10.1016/j.neuron.2020.03.031.

Macrophages Expressing GALC Improve Peripheral Krabbe Disease by a Mechanism Independent of Cross-Correction

Nadav I. Weinstock[1,7], **Daesung Shin**[1,7], **Narayan Dhimal**[1], **Xinying Hong**[2], **Eric E. Irons**[3], **Nicholas J. Silvestri**[1], **Chelsey B. Reed**[1], **Duc Nguyen**[4], **Oliver Sampson**[1], **Yung-Chih Cheng**[5], **Joseph T.Y. Lau**[3], **Ernesto R. Bongarzone**[4], **Julia Kofler**[6], **Maria L. Escolar**[6], **Michael H. Gelb**[2], **Lawrence Wrabetz**[1], **M. Laura Feltri**[1,8,*]

[1]Hunter James Kelly Research Institute, Departments of Biochemistry and Neurology, Jacobs School of Medicine and Biomedical Sciences, University at Buffalo, Buffalo, NY 14203, USA

[2]Departments of Chemistry and Biochemistry, University of Washington, Seattle, WA 98195, USA

[3]Department of Molecular and Cellular Biology, Roswell Park Comprehensive Cancer Center, Buffalo, NY 14203, USA

[4]Department of Anatomy and Cell Biology, University of Illinois at Chicago, Chicago, IL 60612, USA

[5]F.M. Kirby Neurobiology Center, Department of Neurology, Children's Hospital Boston, Harvard Medical School, Boston, MA 02115, USA

[6]Department of Pediatrics, University of Pittsburgh School of Medicine, Pittsburgh, PA 15219, USA

[7]These authors contributed equally

[8]Lead Contact

SUMMARY

Many therapies for lysosomal storage disorders rely on cross-correction of lysosomal enzymes. In globoid cell leukodystrophy (GLD), mutations in GALC cause psychosine accumulation, inducing demyelination, a neuroinflammatory "globoid" reaction and neurodegeneration. The efficiency of GALC cross-correction *in vivo*, the role of the GALC substrate galactosylceramide, and the origin of psychosine are poorly understood. Using a novel GLD model, we show that cross-correction

*Correspondence: mlfeltri@buffalo.edu.

AUTHOR CONTRIBUTIONS

N.I.W. and D.S. designed the project, planned and executed the majority of the experiments, analysis, and interpretation of the results. N.D., N.I.S., C.B.R., and O.S. performed experiments. E.E.I. and J.T.Y.L. advised and helped perform flow cytometry. D.N. and E.R.B. performed bone marrow transplant and psychosine measurements. X.H. and M.H.G. performed mass spectrometry for psychosine, GalCer, and cholesterol. Y.-C.C. provided ATF3-GFP mice. J.K. and M.L.E. provided human tissues. L.W. and M.L.F. conceived and designed the project and oversaw the execution, analysis, and interpretation of the experiments. N.I.W. and M.L.F. wrote the paper.

SUPPLEMENTAL INFORMATION

Supplemental Information can be found online at https://doi.org/10.1016/j.neuron.2020.03.031.

DECLARATION OF INTERESTS

E.R.B. is consultant for Lysosomal Therapeutics and for E-escape-Bio. M.L.E. consults for Passagebio and is PI in the development of a treatment for Krabbe disease using HSCT and gene therapy. Neither have had any decision making in this current study.

does not occur efficiently *in vivo* and that *Galc*-deficient Schwann cells autonomously produce psychosine. Furthermore, macrophages require GALC to degrade myelin, as *Galc*-deficient macrophages are transformed into globoid cells by exposure to galactosylceramide and produce a more severe GLD phenotype. Finally, hematopoietic stem cell transplantation in patients reduces globoid cells in nerves, suggesting that the phagocytic response of healthy macrophages, rather than cross-correction, contributes to the therapeutic effect. Thus, GLD may be caused by at least two mechanisms: psychosine-induced demyelination and secondary neuroinflammation from galactosylceramide storage in macrophages.

Graphical Abstract

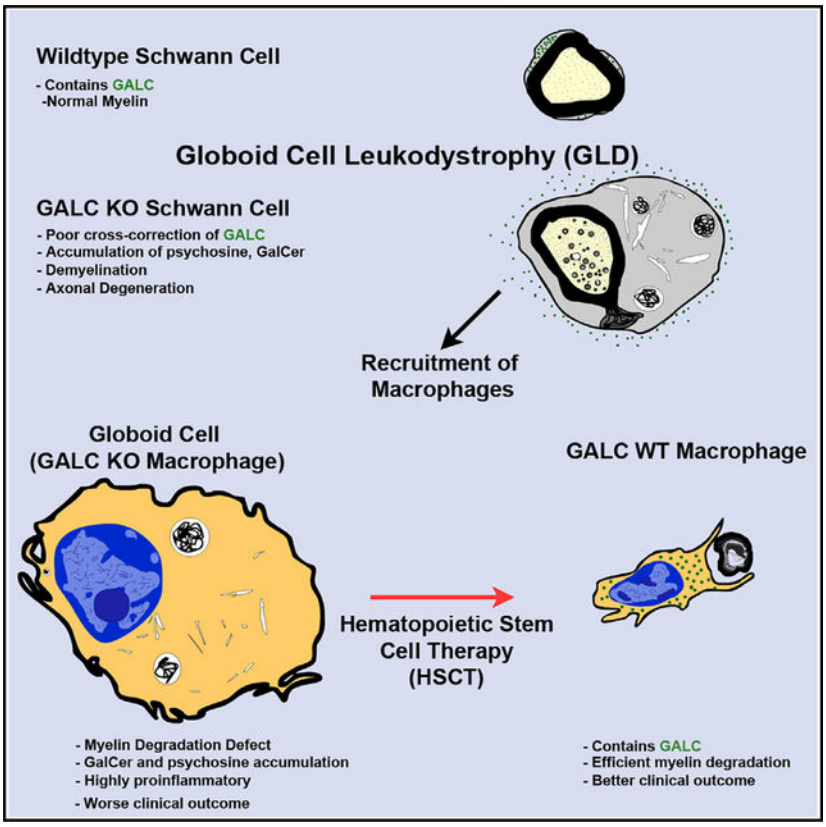

In Brief

Weinstock et al. show that lysosomal GALC is required autonomously by Schwann cells to prevent psychosine formation, demyelination, and subsequent axonal degeneration. Macrophages independently require GALC to serve in phagocytosis and myelin turnover. HSCT likely exerts its therapeutic benefit by restoring phagocyte function rather than cross-correcting myelin cells of GALC.

INTRODUCTION

Globoid cell leukodystrophy (GLD, also Krabbe disease) is a lysosomal storage disorder (LSD) that causes rapid neurological decline and death (Hagberg et al., 1969; Krabbe,

1916). GLD pathogenesis includes intertwined mechanisms of demyelination, neurodegeneration, and inflammation, characterized by the presence of pathognomonic macrophages, globoid cells (Collier and Greenfield, 1924). GLD is caused by mutations in the gene encoding the lysosomal hydrolase galactosylceramidase (*GALC*) (Malone, 1970; Suzuki and Suzuki, 1970), which catabolizes the myelin lipid galactosylceramide (GalCer) and galactosylsphingosine (psychosine) (Li et al., 2019; Miyatake and Suzuki, 1972). Psychosine accumulates in GLD tissues (Svennerholm et al., 1980) and is thought to initiate and drive the majority of GLD pathology (Suzuki, 1998).

The twitcher mouse is a spontaneous *Galc* mutant that mirrors severe GLD (Duchen et al., 1980). Hematopoietic stem cell transplantation (HSCT) extends lifespan in twitcher mice (Yeager et al., 1984) and in pre-symptomatic GLD patients (Escolar et al., 2005). HSCT is thought to work by cross-correction, in which donor-derived cells transfer missing enzyme to *GALC*-deficient cells (reviewed in Sands and Davidson, 2006). This principle is the basis for lysosomal enzyme replacement therapy (ERT) and enhances the “bystander” effect of gene therapy in LSDs. Therefore, cross-correction forms the basis for nearly all approved and prospective clinical therapies among the LSDs.

While many pre-clinical studies have explored delivering *Galc* to GLD models (reviewed in Mikulka and Sands, 2016), cross-correction of GALC *in vivo* is controversial (Kondo et al., 2005; Matthes et al., 2015). Furthermore, although GALC is expressed ubiquitously, its specific role and autonomous function among different cell types is unknown. HSCT may also have immunomodulatory benefits (Hoogerbrugge et al., 1988; Reddy et al., 2011), suggesting an intrinsic role for GALC in leukocytes. We propose that any cell type could, in theory, be directly affected by *GALC* loss of function and may intrinsically contribute to overall GLD progression.

Here, we developed a conditional *Galc* floxed mouse to address these questions using the peripheral nervous system (PNS) as a model system. The PNS is an ideal site to ask questions about cellular autonomy and cross-correction due to its simplicity and anatomical isolation. We found that Schwann cells, the myelinating glia of the PNS, require GALC to maintain myelin and axonal integrity, synthesizing psychosine in its absence. Interestingly, *Galc*-deficient Schwann cells are unable to receive GALC from their surrounding environment due, in part, to ineffective uptake. Furthermore, we discovered that, contrary to expectations, psychosine was not sufficient to drive the entirety of disease burden in GLD. Conversely, macrophages deficient for *Galc* contribute to neurodegeneration by developing a proinflammatory globoid reaction. Thus, we define a novel essential role of GALC in macrophages recruited to sites of demyelination. Based on these data and the analysis of GLD post-mortem human tissues, we propose that the mechanism of HSCT in GLD, and possibly other LSDs, is the restoration of intrinsic degradative functions of macrophages as opposed to cross-correction of neighboring cells.

RESULTS

Galc-Deficient Schwann Cells Are Not Cross-Corrected and Produce Psychosine

We generated a *loxP*-flanked (floxed) *Galc* mouse, to ablate *Galc* in a Cre-dependent fashion. *Galc*-null mice phenocopied *twitcher* mice ($Galc^{W339X/W339X}$) by all tested parameters including survival, weight (Weinstock et al., 2020), and PNS pathology (Figure S1A). *Galc* KO mice express no *Galc* mRNA (Figure 1A), enzymatic activity (Figure 1B), and protein in the sciatic nerve (Figure 1C). We ablated *Galc* in Schwann cells of the PNS (*Galc* SC cKO, Figure S1B) by crossing *Galc* floxed mice to the well-characterized *Mpz*-Cre transgenic line (Feltri et al., 1999). *Galc* SC cKO sciatic nerves had approximately 15% of wild-type (WT) *Galc* mRNA levels (Figure 1D). We suspected that this residual *Galc* mRNA was produced by PNS cells other than Schwann cells. Indeed, primary Schwann cell culture from *Galc* SC cKO produced virtually no *Galc* mRNA (Figure 1E). Thus, *Mpz*-Cre efficiently removed *Galc* expression in Schwann cells.

GALC activity mirrored mRNA levels (Figure 1F), with 80% reductions in *Galc* SC cKO sciatic nerves. Since GALC should be secreted and transferred between cells, we expected that this residual GALC would cross-correct Schwann cells of *Galc* SC cKO. Interestingly, GALC enzymatic activity was nearly absent in *Galc* SC cKO Schwann cell cultures (Figure 1G), and GALC protein was undetectable by immunofluorescence in Schwann cells of nerve teased fibers (Figures 1H and 1I). Furthermore, the toxic GALC substrate psychosine, was elevated to comparable levels in *Galc* SC cKO and *Galc* KO sciatic nerves (Figure 1J; Figure S1C). The cellular identity of the producer of psychosine was previously unknown, and our data first show that Schwann cells are the major producers of psychosine in the PNS. Together, these data illustrate the high efficiency of GALC ablation in Schwann cells of the *Galc* SC cKO mice and show that cross-correction of endogenous GALC to Schwann cells is minimal.

Cross-Correction of GALC Is Perturbed in *Galc*-Deficient Cells

To investigate why cross-correction to Schwann cells was not observed, we performed *in vitro* cross-correction experiments using recombinant human GALC (rhGALC). Primary Schwann cells were cultured from WT and *Galc* KO mice and incubated with His-HA-tagged rhGALC (modified from Shin et al., 2016). Similar to previous reports (Nagano et al., 1998; Rafi et al., 1996), WT Schwann cells were capable of receiving purified rhGALC from media. In contrast, *Galc* KO Schwann cells were five times less efficient at receiving rhGALC (Figures 2A and 2B).

To determine whether this deficiency was true for all *Galc*-deficient cells, similar experiments were performed on mouse embryonic fibroblasts (MEFs) from WT and twitcher mice. MEFs were plated in a Boyden chamber in direct contact with medium from HEK cells transfected with hGALC-HA (Figure 2C) (Shin et al., 2016). Again, cross-correction of hGALC to WT MEFs was more efficient than to twitcher MEFs (Figure 2D). Similarly, human fibroblasts isolated from late-onset and early-infantile GLD patients (Shin et al., 2016) received less GALC than controls (Figure 2E). Notably, the mechanism of GALC cross-correction was also perturbed. Control cells received GALC via mannose-6-phosphate

(M6P)-dependent uptake, as it was competitively inhibited by co-incubation with M6P (Figure 2E). Instead, patient fibroblasts were still able to uptake some GALC, after co-incubation with M6P (Figure 2E). This suggests that GLD fibroblasts may have reduced GALC uptake via the canonical M6P pathway and may have alternative and inefficient compensatory uptake via other mechanisms.

Finally, to determine whether poor *in vivo* cross-correction also occurs in myelinating glia of the CNS, oligodendrocyte *Galc* cKO (*Galc* Oligo cKO) animals were generated by crossing *Galc* floxed mice to *CNPase*-Cre mice (Lappe-Siefke et al., 2003). WT oligodendrocytes of the corpus callosum and cervical spinal cord both express GALC (yellow arrows, Figure 2F; Figure S2). In contrast, most oligodendrocytes in *Galc* Oligo cKO brains and spinal cords did not contain GALC (Figure 2F, red arrows, and Figure S2), indicating that they also were not able to receive extracellular GALC.

GALC Protects Schwann Cells from Demyelination

The PNS is severely affected in GLD and may underlie the refractory morbidity and mortality of HSCT-treated patients (Wright et al., 2017). Despite this, the extent of disease contribution attributable to Schwann cells or the PNS as a whole is unknown. We thus compared peripheral nerve function in *Galc* SC cKO and *Galc* KO mice to define the degree of neuropathy directly attributable to Schwann cell dysfunction.

Galc SC cKO mice develop a clenching phenotype, suggestive of peripheral neuropathy (Figure 3A) and exhibit poor rotarod performance (Figure 3B). *Galc* SC cKO mice survived normally to at least 1 year of age (data not shown) and had only minor reductions in weight (Figure 3C), suggesting PNS dysfunction does not explain the clinical demise and death seen in KD patients.

By electrophysiological studies at P35, ubiquitous *Galc* KO mice exhibited severe reductions in nerve conduction velocity, indicative of myelin defects (Figures 3D and 3E); proximal and distal amplitude, indicative of axonal defects (Figure 3F); and increased latency (Figure 3G). *Galc* SC cKO mice exhibited similar reductions in nerve conduction velocity, suggesting comparable peripheral demyelination but had improved amplitude and latency measurements, implying GALC expression in other cells (i.e., neurons, macrophages) is important for axonal function. Therefore, *Galc* SC cKO animals have a clear neuropathic phenotype, though less severe than full *Galc* KO animals.

Reconstructions of P35 sciatic nerves (Figure 3H) semithin sections show that *Galc* SC cKO nerves were edematous and larger than WT nerves, though not to the degree of full *Galc* KO nerves, reflected in reduction of total axon count and myelinated axon density (Figure 3I). *Galc* KO and *Galc* SC cKO fibers had thin myelin, but *Galc* SC cKO myelin was thicker than *Galc* KO (Figures 3J and 3L). Likewise, *Galc* SC cKO fibers had other GLD pathologic findings, including myelin abnormalities (Figure 3J, blue arrows, Figure 3M), demyelinated fibers (Figure 3J, red arrows, Figure 3N), and degenerating axons (Figure 3J, yellow arrows, Figure 3O). Although qualitatively similar, the occurrence of these features was reduced in *Galc* SC cKO nerves. The attenuated GLD phenotype is particularly surprising when

considering that both genotypes had near-absent GALC activity in Schwann cells and equal levels of the toxic GALC substrate psychosine.

Electron microscopy (EM) of sciatic nerves (Figure 3K) revealed that Schwann cells in both *Galc* SC cKO and *Galc* KO nerves accumulate myelin ovoids and autophagosomes (Figure 3K, blue arrows) encircled in double membranes (Figure S3A) and crystalloid inclusions that were proposed to consist of the GALC substrate galactosylceramide (Figure 3K, orange arrows, Figure S3B) (Austin, 1963; Jacobs et al., 1982; Yunis and Lee, 1970). Interestingly, myelin autophagosomes (Figure 3P) and crystal inclusions (Figure 3Q) accumulate to equal levels in Schwann cells of the *Galc* SC cKO and full *Galc* KO. In contrast, GalCer levels were reduced in *Galc* SC cKO nerves (Figure S3C), as previously reported, possibly representing loss of myelin, or that crystallized GalCer is insoluble by conventional purification techniques. Alternatively, inclusions may be cholesterol crystals formed after myelin degradation (Cantuti-Castelvetri et al., 2018). However, cholesterol did not accumulate in Schwann cell cultures of *Galc* SC cKO (Figure S3D), and cholesterol pathway genes were not uniformly changed to indicate a defect in cholesterol homeostasis (Figure S3E).

Taken together, these data suggest that the absence of GALC in Schwann cells directly accounts for demyelination and the accumulation of psychosine and crystals. However, some other cell type(s) that expresses GALC ameliorate GLD neuropathology in a psychosine-independent manner.

Deletion of GALC in Schwann Cells Causes Progressive Axonal Degeneration

To determine whether ablation of *Galc* in Schwann cells is sufficient to perturb axonal health, we analyzed older *Galc* SC cKO mice (Figure 4). The diameter of *Galc* SC cKO sciatic nerves continued to enlarge (Figure S4). The number of myelinated fibers progressively declined as *Galc* SC cKO mice aged (Figures 4A and 4B), while demyelinated axons (Figure 4C), degenerated axons (Figure 4D) and onion bulbs (Figures 4A and 4E) progressively increased. The etiology of axonal pathology in GLD has been difficult to elucidate, as GALC may play a cell-specific role in both Schwann cells and neurons, and many studies documented a direct effect of psychosine on the neuronal cytoskeleton and on axonal transport (Cantuti Castelvetri et al., 2013; Castelvetri et al., 2011). The progressive fiber loss in *Galc* SC cKO mice suggests that primary Schwann cell dysfunction directly contributes to axonal degeneration.

To more sensitively evaluate axonal integrity, we crossed our mutants to Thy1-YFP mice (Ey et al., 2007). Both *Galc* KO and *Galc* SC cKO nerves had axonal varicosities at P35 (Figure 4F, arrows), though more severe in *Galc* KO (Figure 4G). As mice aged, *Galc* SC cKO developed progressive axonopathy (Figures 4G and 4H) and overt axon degeneration (Figure 4I). To assess neuronal health, we used *Atf3*-GFP transgenic mice that report ATF3 expression in stressed neurons (Seijffers et al., 2006) (Y.-C.C. and C. Woolf, unpublished data). Consistent with the axonopathy data, P60 *Galc* SC cKO mice had more ATF3-GFP$^+$ motor and dorsal root ganglia (DRG) neurons than WT (Figure 4J). Finally, we assessed the localization of nodal proteins. In *Galc* SC cKO axons the structural proteins neurofascin and Caspr, and the functional Na^+ and K^+ channels (Figures 4K and 4L) were diffused and not

well clustered at nodes and paranodes. The abundance of heminodes (Figure 4K, double arrowhead) suggests that the underlying mechanism is segmental demyelination. Taken together, these data suggest that axonal degeneration and neuronal dysfunction can be, at least in part, directly caused by loss of function of Schwann cell GALC. However, GALC absence in neurons or other cell types of the *Galc* KO mice likely accelerates the axonopathy (Castelvetri et al., 2011).

Macrophages Recruited by Schwann Cells Express GALC and Assist in Myelin Turnover

We hypothesized that *Galc* SC cKO mice had attenuated pathology due to the presence of GALC in macrophages. Semithin sections of P35 sciatic nerves showed that macrophages in the *Galc* KO, but not those in *Galc* SC cKO nerves, had a hypertrophic globoid phenotype and many organelles throughout their distended cytoplasm (Figure 5A). Staining for the macrophage marker F4/80 and western blot for macrophage transcription factor PU.1 confirmed that macrophages were more abundant in *Galc* KO sciatic nerves (Figures 5B–5D).

Macrophages are recruited to injured nerves upon fibroblast production of the chemoattractant protein MCP-1 in response to Schwann cell demyelination (reviewed in Martini and Willison, 2016). Interestingly, *Galc* SC cKO and *Galc* KO sciatic nerves had similar levels of MCP-1 (Figure 5E), suggesting that the macrophage recruiting signal is similar in both genotypes. However, the pro-inflammatory cytokines tumor necrosis factor alpha (TNF-α) and interleukin-10β (IL-1β) were increased in *Galc* KO nerves compared to *Galc* SC cKO and WT nerves, respectively (Figure 5E). Thus, macrophages are more abundant and larger and may have a greater inflammatory response in *Galc* KO than in *Galc* SC cKO nerves.

GALC staining from P35 sciatic nerves show that nerve macrophages express GALC in *Galc* SC cKO nerves (Figure 5F, arrowheads). Of note, while globoid cell macrophages from *Galc* KO nerves had abundant $LAMP1^+$ lysosomes, indicative of lysosome storage, Galc-expressing macrophages in the *Galc* SC cKO nerve did not (Figure 5F). By ultrastructural EM, we found that *Galc* KO macrophages accumulate myelin phagosomes and crystalloid inclusions (Figures 5G and 5H), similar to *Galc*-ablated Schwann cells. *Galc* SC cKO macrophages, on the other hand, rarely accumulate crystals, even as mice aged to 6 months (Figures 5G and 5H).

The differences among these macrophages led us to explore their phenotypic signature by flow cytometry. We first analyzed $Cd11b^+$ myeloid cells from the spleen (Figure S5A), a primary lymphoid organ that serves as a reservoir for circulating monocytes and resident macrophages (Swirski et al., 2009). Consistent with previous reports (Galbiati et al., 2007), *Galc* KO spleens were smaller than WT littermates (Figure S5B), previously attributed to autonomic dysfunction. Interestingly, *Galc* SC cKO spleens were instead larger, suggesting a CNS-dependent atrophic mechanism in GLD. Monocytes in *Galc* KO spleens were reduced, dendritic cells were increased, while macrophages remained unchanged (Figure S5C) and expressed similar amounts of the activation markers CD86 and major histocompatibility complex (MHC) II (Figure S5D) and the monocyte marker Ly6C (Figure S5E). This

suggests that the phenotypic signature of circulating macrophages of the *Galc* KO mouse remains naive and is comparable to WT and *Galc* SC cKO macrophages.

In nerves, the majority of $CD11b^+$ myeloid cells were $F4/80^+$ macrophages (Figures S5F and S5G). *Galc* SC cKO and *Galc* KO nerve macrophages expressed similar M1 and M2 markers (Figure S5I). Interestingly, *Galc* KO macrophages expressed high levels of Ly6C (Figure 5J) and low levels of CD206 (Figure 5K). $Ly6C^{hi}$ monocytes are recruited to inflammatory environments and differentiate to $Ly6C^{hi}$ macrophages, where they degrade scar tissue, phagocytose inflammatory debris, and subsequently transition to a more restorative $Ly6C^{low}$ subtype (Ramachandran et al., 2012). Conversely, CD206 renders macrophages phagocytosis competent (Schulz et al., 2019) and is downregulated in globoid cells from *twitcher* CNS (Kondo et al., 2011). Therefore, $Ly6C^{hi}/Cd206^{low}$ *Galc* KO macrophages likely represent dysfunctional macrophages with impaired phagocytosis. Overall, these data suggest that macrophages expressing GALC are recruited to nerves to assist in myelin degradation. When these macrophages do not express GALC (i.e., in the *Galc* KO), they accumulate lysosomes and myelin phagosomes and develop a globoid appearance and an inflammatory and less phagocytic $Ly6C^{hi}/Cd206^{low}$ profile.

Concurrent GALC Ablation in Schwann Cells and Macrophages Recapitulates Peripheral GLD

To directly probe GALC necessity in macrophages, we generated macrophage knockout mice (*Galc* Mac cKO) using LysM-Cre. LysM-Cre mice crossed to tdTomato reporter mice showed that 80% of spleen macrophages and 90% of sciatic nerve macrophages (Figures S6A and S6B) expressed tdTomato, indicative of high recombination efficiency in resident macrophages of the sciatic nerve. Instead, LysM Cre recombination in microglia was specific but less efficient at approximately 35% (Figures S6C and S6D). *Galc* mRNA was not reduced in desheathed *Galc* Mac cKO nerves, likely due to the low number of resident macrophages in non-pathologic nerves (Figure S6E). However, GALC expression by immunofluorescence was reduced in macrophages of the *Galc* Mac cKO (Figures 6A and 6B). *Galc* Mac cKO nerves had normal morphology in EM sections (Figure 6E). These data indicate that GALC is not required in macrophages for myelination nor for the myelin remodeling associated with development and early maintenance.

To ask whether GALC was required in macrophages during demyelination in the context of GLD, we generated *Galc* SC and macrophage double knockouts (*Galc* SC, Mac dKO). Globoid-like macrophages from *Galc* KO sciatic nerves expressed tdTomato when crossed to LysM-Cre;tdTomato(tg) mice (Figure S6F). *Galc* mRNA and protein levels were significantly reduced in the *Galc* SC, Mac dKO, confirming that a large part of GALC expression in the SC cKO is derived from infiltrating macrophages (Figures 6A–6C). The sciatic nerve diameter of P35 *Galc* SC, Mac dKO nerves was larger than P35 *Galc* SC cKO nerves (Figure 6D), suggesting additional pathology. Indeed, macrophages of the *Galc* SC, Mac dKO were larger and more abundant than those of the *Galc* SC cKO (Figures 6A, 6B, and 6E), closely resembling the globoid macrophages of the *Galc* KO by EM (Figure 6G). *Galc* SC, Mac dKO macrophages accumulated myelin phagosomes and crystalloid inclusions, while macrophages of the *Galc* Mac cKO did not (Figures 6F–6H). Furthermore,

macrophages of the *Galc* SC, Mac dKO were Cd206^{low}, like *Galc* KO macrophages, while *Galc* Mac cKO macrophages were Cd206^{hi}, like WT macrophages (Figures 6I and 6J). These data suggest that globoid cell formation is driven by concomitant macrophage GALC deficiency and macrophage exposure to myelin containing GALC substrates from demyelinating cells.

Interestingly, the total nerve pathology of *Galc* SC, Mac dKO was worse when compared to the single *Galc* SC cKO nerve and even approached the pathology of full *Galc* KO. Specifically, the G-ratio, number of demyelinated axons and number of myelin abnormalities all were worse in the *Galc* SC, Mac dKO compared to the *Galc* SC cKO alone (Figures 6E and 6K). Similarly, the amount of axonal degeneration was increased in *Galc* SC, Mac dKO mice (Figures 6E and 6K), and they performed worse on the rotarod (Figure 6L), though LysM-Cre expression in microglia could contribute to this particular test. To assess the long-term functional consequence of GALC ablation in Schwann cells and macrophages, we analyzed 6-month-old mice by nerve conduction studies (Figure S7). Analogous to P35 data, 6-month-old *Galc* SC cKO nerves had robust NCV defects but sparred proximal amplitude function (Figure S7). Instead, *Galc* SC, Mac dKO nerves had impairments in proximal amplitude and delays in latency compared to *Galc* SC cKO nerves. This suggests that the recruitment of GALC-expressing macrophages to sites of demyelination is beneficial to the health of Schwann cells, myelin turnover, and ultimately neuronal andaxonal health and function, while the recruitment of GALC-deficient macrophages further aggravates pathology.

Galc KO Macrophages Have Defects in Myelin and GalCer Degradation

Galc SC, Mac dKO mice highlight the importance of GALC in macrophages recruited to GLD nerves. However, it remains unclear why macrophages need GALC to reduce neuropathology and as to whether the globoid cell reaction occurs in response to the GALC substrate GalCer or psychosine.

To elucidate the cellular mechanism of GALC deficiency in macrophages, we turned to *in vitro* bone-marrow-derived macrophages (BMDMs) cultured from WT or *Galc* KO mice. To test the ability of *Galc* KO macrophages to digest myelin, BMDMs were incubated with IgG-opsonized myelin for 3 h and analyzed thereafter. Western blots of the myelin proteins PMP2 and MPZ showed that *Galc* KO BMDMs accumulated more non-degraded myelin compared to WT BMDMs (Figure 7A). To confirm that this myelin degradation defect was due to the degrading capacity of lysosomes, we repeated the assay in the presence of the proteasome inhibitor bortezomib and found that the myelin degrading capacity of *Galc* KO BMDMs became 5-fold worse than WT BMDMs (Figure 7B). Conversely, when we tested proteasome function of BMDMs by repeating the assay with the lysosome inhibitor chloroquine, *Galc* KO BMDMs degraded myelin proteins at approximately the same rate as WT BMDMs (Figure 7B). Therefore, GALC is required by macrophages for efficient degradation of myelin via the lysosome.

To determine whether GalCer causes globoid-like changes in macrophages, BMDMs were cultured with 20 μM C8-galactosylceramide (GalCer) for 24 h. WT BMDMs cultured with GalCer exhibited an activated morphology after 24 h (Figure 7C). Strikingly, *Galc* KO

BMDMs incubated with GalCer developed a distended globoid-like morphology (Figures 7C and 7D). Immunofluorescence for GalCer and quantification using mass spectrometry showed that GALC KO BMDMs, but not WT BMDMs, accumulated GalCer (Figures 7E and 7F). Psychosine levels in GalCer-treated BMDMs were also increased in *Galc* KO cells, likely due to direct conversion of GalCer to psychosine by acid ceramidase (Li et al., 2019). Psychosine was equally toxic in WT and KO macrophages, while GalCer was not (Figures S8A and S8B). Interestingly, GALC KO BMDMs treated with C8-GalCer, but not psychosine, recapitulated a globoid cell profile including reduced CD206 and increased TNF-α and IL-1β (Figure 7H). Similar findings were seen for markers of the integrated stress response (Figure 7H). Taken together, these data indicate that *Galc* loss of function in macrophages causes a lysosomal defect in degrading myelin, which in turn results in GalCer accumulation and psychosine production, ultimately causing cellular stress and a pro-inflammatory globoid reaction.

HSCT Reduces Globoid Cells in Early Infantile Krabbe Disease

HSCT is beneficial to pre-symptomatic patients with early infantile Krabbe Disease (EIKD). Semithin sections from nerves of transplanted EIKD patients harboring the homozygous 30 kb deletion (Table S1) show improvements in axonal integrity and myelin thickness (Figures 8A and 8A′). The mechanism of action of HSCT is thought to be via secretion of GALC by monocytes or macrophages and uptake by myelinating glia (cross-correction). Our data suggest that GALC may not be able to efficiently transfer from macrophages to pathologic myelinating glia. To confirm this, we performed HSCT on twitcher mice (Figures S9A–S9Z) and asked whether Schwann cells were incorporating GALC. Only a minority of $GALC^+$ macrophages were found in sciatic nerves (Figures S9K and S9L), probably reflecting the low engraftment using this method (Marshall et al., 2018). $GALC^+$ macrophages had fewer lysosomes and expressed CD206 (Figures S9R–S9Z′). Only occasional Schwann cells showed scant GALC reactivity, suggesting that cross-correction may occur but to inefficient levels (Figures S9M–S9Q′). We hypothesized, instead, that $GALC^+$ HSCT-derived macrophages are able to better degrade myelin and benefit GLD by decreasing the GalCer and psychosine load and by immunomodulation. To ask whether this hypothesis is consistent with findings in humans, nerves were stained with the CD68 macrophage marker. Untreated EIKD nerves had widespread macrophage infiltration with globoid appearance (Figure 8B). Strikingly, the EIKD subject who received HSCT had drastically reduced macrophages, suggesting reduced neuroinflammation (Figure 8B). These phenotypes occurred independently of patient lifespan. Furthermore, EM showed that Schwann cells of both untreated and treated EIKD patients had crystal inclusions (Figure 8C), while only macrophages of the untreated subject were globoid with crystalloid inclusions (Figure 8D). Overall, these data suggest that patients with EIKD who receive HSCT have healthy macrophages and few globoid cells. Finally, analysis of nerves from late-onset KD (LOKD) patients show that nerve macrophages are reduced and not globoid in appearance (Figure S9A′). This would suggest that a minimal amount of GALC activity (typically estimated to be between 1% and 5% of control levels) may be sufficient to prevent a globoid reaction. Accordingly, one might suspect that the storage-induced inflammatory reaction might be a major differentiator between EIKD and LOKD.

DISCUSSION

Cellular Cascade of GLD

Demyelination, neurodegeneration, and inflammation are the hallmarks of GLD. Due to the ubiquitous nature of GALC, previous studies were unable to discern whether these events follow in a linear and sequential cascade or instead reflect intertwined mechanisms, each requiring cell autonomous GALC. By using a conditional mutagenic approach in the PNS, we developed a simplified model system to study cellular autonomy of GALC in myelinating glia and the innate immune system. Our initial characterization revealed that GALC is essential to prevent demyelination in Schwann cells and is independently required for proper functioning of injury-recruited macrophages.

Autonomous *Galc* ablation in Schwann cells generates the majority of nerve psychosine in GLD, which is accompanied by widespread demyelination. Degenerating myelin and crystals also accumulated in Schwann cells. This confirms that myelinating glia require GALC for long-term myelin stability. Furthermore, Schwann cell GALC is also required for protection of axonal and neuronal health, at least in part independent of GALC expression in neurons.

Despite near-total ablation of Schwann cell *Galc*, resulting in identical levels of psychosine to the global *Galc* KO nerves, the overall degree of pathology was incomplete in mice with Schwann cell-restricted *Galc* deletion. Many neuropathic features, including demyelination and axonal degeneration, were reduced. On the contrary, pathologic features relating to macrophage function, including storage-laden globoid cells and inflammation, were pointedly absent when *Galc* remained expressed in macrophages. This led us to demonstrate that macrophages require GALC for autonomous functions during demyelination but not during normal nerve development.

During demyelination, as in *Galc* SC cKO nerves, macrophages that express GALC are recruited to assist in myelin degradation. These macrophages are beneficial to overall nerve health. Instead, when injury-recruited macrophages lack GALC, they have a molecular profile associated with poor phagocytosis and are unable to efficiently degrade myelin. This leads to lysosomal dysfunction and the accumulation of galactosylceramide, some of which is converted to psychosine. The ultimate consequence of this process is a proinflammatory globoid cell reaction with further myelin and axonal pathology. These findings are consistent with recent data suggesting that *GALC* haploinsuffiency perturbs remyelination and is a risk factor in multiple sclerosis (Sawcer et al., 2011; Scott-Hewitt et al., 2017).

Psychosine and GalCer Toxicity

Since the advent of the psychosine hypothesis (Miyatake and Suzuki, 1972), the Krabbe field has explored numerous mechanisms and pathways by which psychosine causes toxicity, including a direct effect on neuronal health (reviewed in Spassieva and Bieberich, 2016). We thus expected that psychosine would be toxic to surrounding cells. We were surprised, therefore, when pathology did not directly correlate with psychosine levels. This suggests that a non-psychosine-based GLD mechanism exists to explain the full pathology. Because psychosine levels in global KO and in Schwann cell-specific cKO nerves were

similar, psychosine, once generated, may not be readily degraded by other GALC-expressing cells in the endoneurium. Alternatively, psychosine may not be freely diffusible between cells, even if the fact that psychosine is found in circulating blood may argue otherwise.

The pathogenic role of the major GALC substrate GalCer is unclear. Presumed GalCer inclusions are found in lysosomes of GLD globoid cells, oligodendrocytes, and Schwann cells (Suzuki and Grover, 1970; Yunis and Lee, 1970). Furthermore, direct implantation of GalCer, but not psychosine, in WT rat brains produced a “globoid reaction” (Andrews and Menkes, 1970). Ultimately though, GalCer does not accumulate at a whole tissue level (Hers, 1965) in brain or nerve (Suzuki, 1998) and has not been shown to be toxic in culture. Our work argues that GalCer nonetheless plays an important part in GLD toxicity. We saw that GalCer was sufficient to induce a globoid reaction in GALC-deficient BMDMs. Induced globoid cells expressed more proinflammatory cytokines and effectors of the integrated stress response. Remarkably, GALC-deficient macrophages *in vivo* have decreased expression of CD206, a surface receptor that enables macrophage phagocytosis (Schulz et al., 2019) and short-term GalCer induction in *Galc*-deficient BMDMs was sufficient to decrease CD206 expression, suggesting a direct role of GalCer in impairing macrophage function. Crystal accumulation in cells and particularly innate immune cells can be toxic due to the formation of the NLRP3 inflammasome (Duewell et al., 2010; Rajamäki et al., 2010) or lysosome membrane permeabilization (Ono et al., 2018), such as in gout (Martinon et al., 2006), asbestos, silica lung disease (Dostert et al., 2008), and atherosclerosis (Duewell et al., 2010). Similarly, myelin-derived crystals, thought to be composed of cholesterol, induce pathology in a demyelinating model (Cantuti-Castelvetri et al., 2018). Therefore, a number of GalCer-based toxicities could occur in GLD.

GALC Cross-Correction

A major finding of our study is that endogenous GALC was unable to efficiently cross-correct *Galc*-deficient cells *in vivo*. Furthermore, we found that *Galc* deficiency impaired the uptake of GALC in Schwann cells, oligodendrocytes, MEFs, and human fibroblasts. These data are surprising, especially because cross-correction is considered the basis for a number of therapies of LSDs (reviewed in Coutinho et al., 2012; Sands and Davidson, 2006). The majority of previous cross-correction studies have been analyzed *in vitro* and have, with a few notable exceptions, rarely compared the uptake ability of WT cells to their disease mutant counterparts (Kondo et al., 2005; Luddi et al., 2001; Nagano et al., 1998; Rafi et al., 1996). These data may also explain why Fabry disease females with one mutant copy, once thought to be “carriers” may develop clinical findings despite significant αGAL protein present (MacDermot et al., 2001; Wilcox et al., 2008). In addition, a recent study in postmortem brains from HSCT-treated metachromatic leukodystrophy patients also showed no evidence of cross-correction (Wolf et al., 2020). Whether this phenomenon extends to other LSDs remains an important unanswered question and may explain why certain corrective therapies have had only modest clinical improvements despite overall increased enzymatic activity.

HSCT for GLD

HSCT is the mainstay of treatment for pre-symptomatic KD. The mechanism of action for HSCT is poorly understood and is generally attributed to cross-correction, though immunomodulatory benefits of HSCT have also been proposed (Hoogerbrugge et al., 1988; Reddy et al., 2011). Our mouse data argue against the notion that donor-derived cells efficiently cross-correct neuronal and peripheral glial cells. Instead, we propose that allogenic transplantation restores the beneficial function of GALC-expressing macrophages and microglia in GLD, thereby reducing substrate accumulation and disease burden. In line with these findings, analysis of nerves from early infantile KD patients showed that HSCT normalized the number and globoid morphology of peripheral macrophages. This correlated with slightly decreased neuropathic findings in nerves from HSCT-treated patients, that were strikingly similar to the differences found between *Galc* SC cKO and *Galc* SC, Mac dKO nerves.

STAR★METHODS

RESOURCE AVAILABILITY

Lead Contact—Further information and requests for resources and reagents should be directed to and will be fulfilled by the lead contact, M. Laura Feltri (mlfetri@buffalo.edu).

Material Availability—There are no restrictions on any data or materials presented in this paper. All unique/stable regents generated in this study, including plasmids generated, are available from the Lead Contact with a completed Materials Transfer Agreement. Floxed *Galc* mice are freely available from the Lead Contact and D. Shin (daesungs@buffalo.edu).

Data and Code Availability—No dataset/code is associated with this paper.

EXPERIMENTAL MODEL AND SUBJECT DETAILS

Animals—All mice were maintained in C57BL/6 background (Charles River Laboratories International, Inc.). Both male and female mice were used in all experiments. Animal housing and experimentation strictly adhered to Department of Laboratory and Animal Resource (DLAR) core facility at Roswell Park Cancer Institute (RPCI), and both RPCI and UB Institutional Animal Care and Use Committee protocols (IACUC approval UB# 1188 and 1254M). DNA was extracted from toe clippings or ear punching. *Galc* floxed mice were designed by L.W. and D.S. and generated by D.S. (Weinstock et al., 2020). *Galc* twitcher mice (JAX#000845) (Duchen et al., 1980) were used in comparison to validate *Galc* knockout (KO) mice. To produce *Galc* KO mice resembling twitcher mouse, *Galc* floxed mice were crossed with CMV-Cre (JAX# 006054) (Schwenk et al., 1995). Recombination of the floxed allele was passed in the germ-line of these mice, separated from Cre expression, and defined as a null allele (denoted by " − "). P0-Cre (JAX#017927) mice were used to produce recombination in Schwann cells (Feltri et al., 1999). LysM-Cre (JAX#004781) mice were used to produce recombination in macrophages (and granulocytes) (Clausen et al., 1999). CNPase-Cre mice were used to produce recombination in oligodendrocytes (Lappe-Siefke et al., 2003). Td-Tomato Mice (JAX#007905) were used to test Cre specificity by expression of tdTomato fluorescence (Madisen et al., 2010). For a detailed characterization

of neuronal/axonal morphology, the reporter Thy1.1-YFP mouse (JAX# 003709), which expresses YFP in subsets of neurons, allowed the fluorescent labeling of their projecting axons (Porrero et al., 2010). ATF3-GFP Mice (Y.-C.C. and C. Woolf, unpublished data) express GFP under control of the neuronal stress marker ATF3.

Human Tissues—Parents of Krabbe disease patients consented to autopsy and tissue donation to the University of Pittsburgh Pediatric Neurodegenerative Brain Bank. All banking procedures were approved by the Committee for Oversight of Research and Clinical Training Involving Decedents (CORID) at the University of Pittsburgh. The University of Buffalo granted an IRB exemption for the analysis of post-mortem human samples. Subject information of patient tissues used in this study can be found in Table S1.

Cell Culture—Primary Schwann cell culture were prepared from sciatic nerves dissected from P10-P15 mice (or from other ages if specified) under aseptic conditions. Nerves were placed in Leibovitz L-15 media supplemented with penicillin/streptomycin. Nerves were desheathed of epineurium and then transferred to high glucose DMEM supplemented with in 0.25% dispase II and 0.05% collagenase. Nerves were physically dissociated and incubated at 37C, 5%CO2 for 24 hours. Media and tissue was pipetted for further dissociation and transferred to plates pre-coated with poly-L-lysine and Laminin 211. Cells were filtered through a 70 μm cell strainer, plated in concentrated bubbles, and incubated for 24 hours. The following day, media and debris were removed and cells were grown in DMEM media supplemented with N2, penicillin/streptomycin, FBS and L-glutamine for 3–4 days in culture.

For bone marrow derived macrophages, isolation was performed using a previously published protocol (Weischenfeldt and Porse, 2008). 5-week-old mice were sacrificed by cervical dislocation. Femurs and tibias are collected without breaking bones, using sterile technique. Bone marrow was flushed using ice cold PBS, centrifuged, and resuspended in BMDM-complete media (RPMI 1640, 10% FBS, 1% glutamine, 1% Penicillin/ Streptomycin, and 200 ng/mL rm-CSF). Bone marrow collected cells were plated on bacterial grade cell culture plates and grown at 37°C in 5% CO2 for 5 days. BMDMs were then scraped and replated on cell culture grade plastic dishes in BMDM-complete media. Cells were ready for downstream applications after 24 hours.

Mouse embryonic fibroblasts (MEFs) were collected according to previously published protocol (Durkin et al. Bio-protocol 2013). Human GLD and control fibroblasts were purchased from Telethon biobank and cultured as previously published (Shin et al., 2016). HEK293T cells, MEFs and human fibroblasts were grown in DMEM supplemented with 10% FBS, 1% glutamine, 1% penicillin/streptomycin (Shin et al., 2016). Nerve-derived macrophages were isolated as described in the Flow Cytometry section.

METHOD DETAILS

Isolation of Genomic DNA—For routine genotyping, toes were digested in 75 μL 25mM NaOH / 0.2 mM EDTA at 95°C for 45 minutes, and neutralized with 75 μL of 40 mM Tris HCl (pH 5.5). Samples were centrifuged and used for PCR reactions. For recombination PCRs, tissues were dissected and digested at 50°C overnight in 500 μL SNET buffer (20mM

tris-Cl pH 8.0, 5mM EDTA pH 8.0, 400 mM NaCl, 1% w/v SDS) and 10 μL of proteinase K (PK, 20mg/mL in H_2O). 500 μL of Phenol/Chloroform (1:1) was then added, vortexed and centrifuged. Supernatants were collected and 2x volume of 100% ethanol was added and centrifuged. Pellets were washed with 70% ethanol, dried, and resuspended in autoclaved double distilled H20.

RNA Isolation—Total RNA was isolated from mouse sciatic nerves using TRIzol reagent following the manufacturers' instruction. For frozen nerves or tissues, samples were frozen in liquid N_2 following dissection and stored at −80°C. A cooled pestle was used to pulverize tissues to powder. Powder was resuspended in TRIzol reagent. For cells, TRIzol was added directly to PBS-washed cell culture plate. After incubation for 5 minutes at room temperature, chloroform was added, shaken vigorously and centrifuged. The upper aqueous phase containing RNA was collected and 1 μL glycogen was added (20mg/mL). RNA was precipitated with isopropanol, pelleted, and washed twice with 75% ethanol. Pellets were resuspend in 10 μL DEPC-dH_2O. RNA was quantified (OD at 260 nm) using a spectrophotometer (Thermo Fisher scientific; nanodrop 2000C) and analyzed for purity by 260/280 ratio.

cDNA Preparation and RT PCR—Invitrogen Kit (Superscript III) was used to convert RNA to cDNA using oligo dT and random hexamers provided. Following RT reaction, provided RNase H was added to each sample. cDNA was collected and stored at −80°C. For RT-PCR, SYBR Green and Taqman systems were used for different primers. For both systems the RT-PCR reaction was 50°C for 3 minutes, 95°C for 10 minutes, 95°C for 15 s, 60°C for 1 minutes (40 cycles). The amount of cDNA used in RT-PCR reactions were determined by standard curves in accordance with Applied Biosystems protocols. Each cDNA sample was tested in triplicate for the presence of each gene of interest and for the standard (*18S* rRNA or β-*actin*) on the same plates. Target and reference gene PCR amplification was performed. Assays on Demands (Applied Biosystems Instruments): *18S* (Hs99999901_s1), *Ddit3*/*Chop* (Mm00492097_m1), *XBP1s* (Mm03464496_m1), *Hspa5*/*BIP* (Hs99999174_m1), *CD206* (Mm01329362_m1). SYBR primers used can be found in Table S2. Mouse *Galc* mRNA primers were designed spanning exons 9 (forward primer) and 10 (reverse primer). All samples were analyzed in triplicate and the relative expression of the target RNAs was calculated using the $\Delta\Delta C_t$ of the gene of interest compared to the housekeeper gene.

GALC enzymatic activity—GALC activity from, tissue or cell culture, was determined by a previously described method (Martino et al., 2009). Tissues and cells were homogenized in 10 mmol/L sodium phosphate buffer pH 6.0 with 0.1% Nonidet NP40 and sonicated.15 μg of protein extract (50 μL) was added to 100 μL of 1.5 mmol/L MUGAL substrate (fluorogenic substrate 4-methylumbelliferyl derivative 4-MU-β-D-galactoside) resuspended in 0.1/0.2 mol/L citrate/phosphate buffer, pH 4.0. 55 μM AgNO3 was also added to the mixture. Reactions were incubated for 30 min at 37°C. Reactions were stopped by adding 50 μL of 0.2 mol/L glycine/NaOH, pH 10.6. Fluorescence was measured using a spectrofluorometer (ex = 360 nm, em = 446 nm; Biotek Cytation5 imaging reader).

Trans-cardiac Perfusion—Brain immunohistochemistry was performed on animals perfused with 4% paraformaldehyde. Mice were anesthetized with avertin and monitored until sedated. Once unconscious, the thoracic wall was removed and the right atria was punctured. 20 mL of PBS was perfused into the left ventricle, followed immediately by 20 mL of 4% PFA. Tissues were post fixed in 4% PFA for 24 hours at 4 C, followed by sucrose and OCT embedding. Tissues were frozen in OCT and stored at −80C.

Immunofluorescence—Nerves were fixed for 30 minutes in 4% paraformaldehyde, washed 2x in PBS for 5 minutes, left overnight in 20% sucrose at 4°C and then frozen in OCT. Longitudinal sections (10 μm) were cut on a cryostat (Leica CM 1950), collected on a slide and circled with raw pap-pen boundary. Sections were rehydrated in PBS for 10 min at room temperature, blocked for 1hr at room temperature in blocking buffer (3% BSA in PBS; 2% normal goat serum, 0.5% Triton X-100). Primary antibodies were either purchased, affinity purified as described previously (GALC (Lee et al., 2010), CASPR (Peles et al., 1997)) or prodced from hybridoma cells (anti-GalCer O1 (Sommer and Schachner, 1981)). Primary antibodies were diluted in blocking buffer and applied to sections for 1 hour, at room temperature, in a humidified chamber. After washing 3x with PBS, secondary antibodies were diluted in blocking buffer and applied to sections for 1 hour at room temperature. DAPI was added for 8 minutes at room temperature. Sections were then washed 3x with PBS and mounted in Vectashield mounting media. Staining for lysosomes (including GALC) was similar to general protocol, but block included 0.05% saponin. Unless otherwise specified, all imaging was processed using Leica confocal microscope (Leica TCS SP5 II, Leica DMI 5000 CS).

Cholesterol Staining, Filipin—Primary Schwann cells were cultured from WT and *Galc* SC cKO nerves from P60 animals as described above. On day 3 of culture Schwann cells grown on coverslips were processed with cholesterol assay kit (abcam), according to manufacturer's directions. Filipin III stock solution was prepared in 100% ethanol. Cell culture medium was removed from wells and cells were fixed with cell-based assay fixative solution for 10 minutes. Cells were washed with cholesterol detection wash buffer, three times, for five minutes each. Filipin stock solution was diluted in cholesterol detection assay buffer and applied to each well for 60 minutes. Cells were washed with wash buffer, twice, for five minutes. Coverslips were mounted on microscope slides with Vectashield and immediately processed on Apotome microscope (Zeiss Observer.Z1 AX10).

Flow cytometry—Spleens of P35 euthanized mice were removed, homogenized between frosted glass slides, flushed through a 70 μm filter, then subjected to ACK lysis in order to remove anucleated cells. Peripheral nerves of P35 mice, including sciatic nerves, trigeminal nerves and brachial plexus nerves, were dissected and pooled together. Pooled nerves were placed in Leibovitz L-15 media supplemented with penicillin/streptomycin. Nerves (with epineurium) were transferred to high glucose DMEM supplemented with in 0.25% dispase II and 0.05% collagenase. Nerves were manually dissociated using forceps and incubated at 37°C, shaking, for 45 minutes. Media and tissue was pipetted for further dissociation and filtered through two sequential 250 μm cell strainers. Both splenic and peripheral nerve cells were blocked for 15 minutes with Fc blocking reagent (anti-CD16/32, clone 93, Biolegend)

in BSA-containing solution to reduce non-specific binding. Cell surface markers were stained with the appropriate combination of antibodies for 20 minutes, washed, and kept on ice. For staining of intracellular antigens, cells were fixed with 2% formalin for 20 minutes at room temperature, permeabilized with Perm/Wash reagent for 15 minutes (BD Cytofix/Cytoperm, BD Biosciences), then stained with appropriate antibodies in Perm/Wash reagent for 30 minutes. All samples were analyzed by BD LSR II flow cytometer. Data was analyzed with FlowJo software against isotype and single color controls. Myeloid cells were identified by positive staining for CD11b. Further subsets were defined as in Figure S8.

Panel 1: CD11b-BV711 (M1/70), Ly6G-PE (1A8), F4/80-APC (BM8), Ly6C-PE/Cy7 (HK1.4), CD11c-FITC (HL-3, BD PharMingen), CD86-APC/Cy7 (GL-1), MHC II-PerCP (M5/114.15.2)

Panel 2: CD11b-BV510 (M1/70), F4/80-APC/Cy7 (BM8), Nos2-APC (CXNFT), Arg1-FITC (IC5868F, R&D Systems), CD206-PE/Cy7 (C068C2), Egr2-PE (erongr2, Invitrogen), TNFa-BV711 (MP6-XT22), IL10-BV421 (JES5–16E3), IL12-PerCP/Cy5.5 (C15.6)

Teased Fiber Preparation—Slides were prepared using vectabond (Tespa). Nerves were fixed in 4% PFA for 30 minutes and then washed 3x with PBS. Nerves were desheathed with forceps and a 27-gauge needle. Bundles of fibers were separated in PBS using 27-gauge needles and then gently teased apart to single fibers on tespa coated slides. Slides were allowed to dry for at least one hour before staining. Staining protocol replicated as above.

Cloning and Purification of rhGALC—*hGALC* cDNA was previously ligated between the BamHI and XhoI sites of the pCMVTag4a vector (Shin et al., 2016) and included an HA tag. This plasmid construct was used for transwell fibroblast experiments. The plasmid was further modified to introduce an in-frame HA-6xHis-STOP at a SalI site by using primers listed in Table S2. The plasmid was sequenced after cloning. HEK293T cells were cultured and transfected with rhGALC-HA-His using lipofectamine 3000 reagent. HEK cells were cultured in serum-free media for 72 hours. Media was collected every 24 hours and stored at 4°C. After 72 hours, media was pooled, filtered and added to columns packed with His-Pur resin. Resin was washed (PBS, 10 mM imadizole) then eluted (PBS, 150 mM imadizole) in 8 mL. Eluant was concentrated using Amicon ultra15 10K columns, 4,000 x *g*, 4°C, 30 min. rhGALC-HA-His was quantified for protein using BCA method. Primary Schwann cells were cultured as described previously. After 4 days in culture, Schwann cells were treated with 5 μg/mL rhGALC-HA-His in serum-free media for 24 hours. Following incubation with enzyme, media was removed and cells were washed. Cells were then collected for western blot analysis. D-mannose 6-phosphate (M6P) (Sigma M6876) was added at a final concentration of 6 mM as described in (Sukehisa Nagano et al., Clinica Chimica Acta 276 (1998) 53–61) to inhibit CI-MPR mediated uptake.

Western Blotting—Tissue or cells were lysed in RIPA buffer supplemented with phosphatase and protease inhibitors. For sciatic nerves, the samples were flash frozen in liquid nitrogen and pulverized with a pestle. The crushed powder was resuspended in lysis buffer. For cells, wells were washed with PBS 1x and RIPA buffer was added to each well on

ice. Cells were scrapped off in RIPA buffer and collected. Lysates were disrupted on a cell homogenizer for 10 minutes at 4°C and left on ice for 20 minutes. Lysates were centrifuged and the supernatant was removed. Protein concentration analysis was determined with a BCA protein assay kit (Thermo Fisher Scientific) according to manufacturer's instructions. Samples were prepared with 6x Laemmli buffer and lysis buffer. 5 μg to 20 μg of protein were loaded per lane and resolved using SDS-polyacrylamide gel electrophoresis (SDS-PAGE) under denaturing conditions with a mini-Protean II gel electrophoresis apparatus and included a Precision Plus Standard Protein Dual color from (Biorad) to enable band size identification. Separated proteins were transferred to a PVDF blotting membrane, in a mini gel transfer tank. Non-specific binding sites on the membrane were blocked for 1 hour at room temperature using 5% non-fat free milk powder in TBS/0.05% Tween 20. Primary antibodies in 3% BSA in TBS/0.05% Tween 20 were incubated overnight at 4°C. Membranes were washed in TBST (0.05%) 3x for 5 minutes and incubated for 1 hour at room temperature with secondary antibody. Secondary antibodies were either horseradish peroxidase-conjugated (HRP) secondary antibody diluted in 5% milk TBST or Li-Cor secondary fluorescent antibody diluted in Li-Cor odyssey buffer. Blots incubated with HRP-conjugated secondary antibody were developed with ECL chemiluminescent reagent with film on a Chemi-doc apparatus (BIO RAD), while Li-Cor antibodies were developed using the Odyssey CLx apparatus. (Li-Cor).

Semithin Morphology and Electron Microscopy—Nerves were dissected and fixed in 2% glutaraldehyde. Nerves were washed in phosphate buffer 0.12M pH 7.4 at RT and incubated in osmium tetroxide 1% (phosphate buffer 0.12M pH 7.4) for two hours in room temperature in the dark. Nerves were then washed twice (phosphate buffer 0.12M pH 7.4) and dehydrated in increasing ethanol concentrations (50%, 70%, 90% and 100%) followed by incubation in propylene oxide. Propylene oxide was then evaporated and nerves were embedded in Epon 100%. Resin was polymerized at 60°C overnight. Nerves were then cut to semithin sections at 1 μm thickness or ultrathin sections at 80–85 nm thickness. Semithin sections were stained with toluidine blue 2% (phosphate buffer 0.12M pH 7.4). Ultrathin sections with saturated uranyl acetate (in dH_2O) and lead citrate.

For quantification of axon density, 10 fields per nerve were imaged and analyzed. For quantification of myelin abnormalities, all axons in cross section of reconstructed sciatic nerves were counted and normalized to total myelinated axons. G-ratio analyses were performed on EM images, in which 75–100 axons were quantified per nerve. For axon degeneration and demyelination, 300 axons were analyzed per nerve, on EM images, and normalized as a percentage of total axons. For myelin ovoid and crystal analysis, Schwann cells and macrophages were assessed on EM micrographs. Schwann cells were identified by presence of basal lamina while macrophages were identified by characteristic morphologic features including microvilli.

Nerve Conduction Studies—Electrophysiologic studies were performed as previously described (Della-Flora Nunes et al., 2017). Mice (35 days or 6 months) were anesthetized with 2,2,2 tribromoethanol (avertin; Sigma-Aldrich) 10mg/mL in H_2O and placed under a heating lamp. The sciatic nerve conduction velocity was obtained with steel monopolar

needle electrodes. One pair of stimulating electrodes was inserted subcutaneously near the nerve at the ankle, a second pair of electrodes was placed at the sciatic notch, and a third pair over the dorsum of the spine. The compound motor action potential (CMAP) was recorded with an active electrode inserted in muscles in the middle of the paw and a reference needle in the skin between the first and second digits.

Rotarod Analysis—Rotarod analyses were performed as previously described (Della-Flora Nunes et al., 2017). All mice were tested in two sessions of three trials each per day (6-hour rest between the two daily sessions) for two consecutive days. Analyses measuring 35 day old animals occurred at P34 and P35; those measuring P60 animals occurred at P59 and P60. Only naive mice were used for Rotarod tests (no training occurred prior to trial 1). Rotarod conditions were set to acceleration of 5 rotations per minute^2, starting at a minimum velocity of 4 rotations per minute and accelerating to a maximum velocity of 40 rotations per minute. Each trial consisted of one acclimating run that was not scored. The next three runs were recorded and averaged. Each run was stopped when the mouse fell or passed completely underneath the rod (180 degrees of rotation).

Pig Myelin Purification—Pig myelin was purified for use in myelin phagocytosis assay. Frozen pig nerves were stored at −80°C until used. Myelin was purified according to (Larocca and Norton, 2006). Pig nerves were pulverized using a mortar and pestle on dry ice. Nerve homogenate was further homogenized in a dounce homogenizer in 0.27 M sucrose solution, containing protease inhibitors. Connective tissue was eliminating by filtering homogenate through a cheese cloth. Equal volumes of nerve/0.27M sucrose solution was overlaid over 0.83M sucrose in ultracentrifuge tubes. The solution was centrifuged for 45 min at 82,000 x *g*, at 4°C. Using a Pasteur pipet, the crude myelin fraction was isolated at the 0.27/0.83M sucrose interface. Osmotic shock was then carried out by resuspending the combined myelin layers in Tris Cl buffer. The myelin/Tris buffer was then ultracentrifuged for 15 min at 82,000 x *g*, at 4°C. The pellet was resuspended in Tris buffer, and the protein concentration was estimated by the BCA method.

BMDM Myelin phagocytosis assays—Experiments were modified from previously described methods (Mosley and Cuzner, 1996; Trotter et al., 1986). Bone marrow derived macrophages (BMDMs) were plated in complete BMDM media. Pig myelin was pre-incubated with rabbit anti-PMP2 antibody (proteintech) and rabbit anti-MPZ antibody (abcam) at a concentration of 0.1 μL/μg of myelin protein, for two hours at 37°C. Opsonized myelin was added to serum free BMDM media at a concentration of 200 μg/mL, and delivered to macrophages for 3 hours. Pharmacologic inhibitors were added to opsonized myelin when indicated. The concentration of bortezomib was 20 nM and the concentration of chloroquine was 100 μM. After assay, cells were washed in PBS and collected for protein analysis.

BMDM GalCer and psychosine treatment—Bone marrow derived macrophages (BMDMs) were plated in complete BMDM media. C8-galacotsylceramide or psychosine was purchased from Avanti polar lipids and resuspended at 10 mM in DMSO. Lipids were aliquoted and stored at −20°C until further use. At use, lipids were warmed in the incubator

for 10–15 min and added to cells in serum-free media for 24 hours. GalCer was delivered at a concentration of 20 μM. Psychosine was delivered at a concentration of 20 μM for cell viability experiments or 5 μM for qPCR experiments. Cells were washed in PBS prior to downstream applications.

Cell Viability Assays—Cells were assessed for cell viability using the cell counting kit 8 (Dojindo) in 96 well plates. After treating BMDMs with lipids (C8-GalCer and psychosine), 10 μL of WST-8 reagent was added to each well. Cells were incubated at 37°C, for 4 hours. Plates were read at 450 nm absorbance on a plate reader and normalized according to manufacturer's instructions.

Bone Marrow Transplantation—WT and twitcher mice were transplanted with bone marrow, as previously described (Marshall et al., 2018). Briefly, P2 mice were injected intravenous treatment of bone marrow stem cells harvested from 6–8 week old syngeneic WT mice (30 million cells each treatment). Mice were sacrificed at P35 and nerves were 4% PFA post-fixed and sucrose embedded as described previously.

Psychosine Measurement—Nerves were snap frozen in liquid nitrogen and stored at −80°C until ready to perform experiments. Nerves were pulverized and homogenized in PBS. A fraction of PBS-homogenate was refrozen and shipped to for analysis by collaborators X.H. and M.G. or intact frozen nerves were sent to D.N. and E.R.B. For the latter, psychosine was quantified according to (Galbiati et al., 2007).

For the former, the other fraction of PBS-homogenate was mixed with 10X RIPA lysis buffer to make 1X RIPA buffer. Samples were then sonicated and analyzed for protein quantification by BCA. To 5 μL of tissue/PBS homogenate, 250 μL of 1 nM d_5-psychosine (Avanti Polar Lipids) in methanol was added. Psychosine was extracted at 37°C for 2 h with orbital shaking (250 rpm). After extraction, the residual was centrifuged at 13,000 x g for 5 min. The supernatant was loaded onto an Oasis MCX column (1 cc, 30 mg, Waters Corp., #186000252), which was preconditioned with 1 mL of methanol, following by 1 mL of water. After sample loading, the cartridge was washed with 1 mL of water with 2% formic acid, 1 mL of methanol, and then 1 mL of 80:20 methanol:water (v:v) with 5% NH_4OH. The column was washed with 0.8 mL of methanol with 5% NH_4OH, which was collected and solvent evaporated using a SpeedVac vacuum concentrator. The residue was stored at −20°C until analyzed. The residue was reconstituted with 100 μL mobile phase prior to UPLC-MS/MS analysis.

For UPLC-MSMS analysis, an ACQUITY UPLC I-Class system from Waters was used for the separation of glucosyl- and galactosyl-sphingosine (psychosine). A 2.1 × 50 mm BEH Amide column (Waters Corp., #186004800) with a guard column (Waters Corp., #186004799) was used. The column was held at 40°C. Mobile phase A was water with 2 mM ammonium acetate and 0.1% NH_4OH, mobile phase B was 95:5 acetonitrile:water (v:v) with 2 mM ammonium acetate and 0.1% NH_4OH. The flow rate was 0.3 mL/min. The weak needle wash was 95:5 acetonitrile:water (v:v), and the strong needle wash was 50:50 acetonitrile: water. Ten μL of sample was injected onto the column, which was developed with the following gradient: elution started with 99.5% mobile phase B, decreased to 95%

mobile phase B over 4.5 min (linear gradient), decreased to 60% mobile phase B at 5.5 min (linear gradient) and was held at 60% mobile phase B for cleaning until 6.0 min. At 6.01 min the solvent was switched back to initial conditions (99.5% mobile phase B) and was held for 9 min for re-equilibration.

The UPLC system was coupled to a Xevo TQ-S (Waters) tandem mass spectrometer, which was operated in the multiple reaction monitoring (MRM) mode. ESI source parameters are as follows: capillary 3.5kV, source temperature 150°C, desolvation temperature 600°C, cone gas flow 50 L/Hr, desolvation gas flow 1000 L/Hr and collision gas flow ON (mL/Min). MRM transitions of psychosine and d5-psychsoine had SRM transition (m/z) of 462.30 > 282.20, and 467.35 > 287.35 respectively. Cone voltage was 20V and collision energy was 21V.

QUANTIFICATION AND STATISTICAL ANALYSIS

Data collection and analyses were performed blind to genotypes and conditions of experiments. Quantification of images and mean fluorescent intensity was done using ImageJ (Schneider et al., 2012). Statistical details of experiments can be found in figure legends, including statistical tests used, value of n and dispersion measures. Additional details may be found in methods and main text.

Statistical tests were performed using GraphPad Prism version 7.00 for Windows, GraphPad Software, San Diego California USA, https://www.graphpad.com/, and included Student t test, One way ANOVA and Two way ANOVA as desribed through text. Statistical significance was defined as $p < 0.05$ and were denoted by asterisks. * = $p < 0.05$, ** = $p < 0.01$; *** = $p < 0.005$; **** = $p < 0.001$. Data throughout text are presented as mean ± SEM.

Supplementary Material

Refer to Web version on PubMed Central for supplementary material.

ACKNOWLEDGMENTS

This work was funded by grants NIH R01 NS111715 to M.L.F. and L.W., NIH R01 NS112327 to D.S., NIH F30 NS090835 to N.I.W., NIH R01NS065808 to E.R.B., the Empire State Development Corporation Krabbe Disease Grants U446 and W753 to L.W., and the Hunter's Hope Foundation. We thank E. Hurley and G.G. Shackleford for expert technical assistance and K. Mincorczyk, A. Lauko, K. Diaz, and I. Yu for their contribution; C. Eckman, Mayo Clinic for anti-GALC antibody; E. Peles, Weizmann Institute for anti-Caspr antibodies; C. Woolf, Harvard Medical School for ATF3-GFP mice; Klaus Nave MPI Gottingen for CNPase Cre mice. We are most grateful to the families who have donated their loved one's tissues, made possible by Partners for Krabbe Research and the NDRD Brain and Tissue Bank, UPMC Pittsburgh PA.

REFERENCES

Andrews JM, and Menkes JH (1970). Ultrastructure of experimentally produced globoid cells in the rat. Exp. Neurol 29, 483–493. [PubMed: 5492920]

Austin JH (1963). Studies in globoid (KRABBE) Leukodystrophy. II. Controlled thin-layer Chromatographic studies of globoid body fractions in seven patients. J. Neurochem 10, 921–930. [PubMed: 14087696]

Cantuti Castelvetri L, Givogri MI, Hebert A, Smith B, Song Y, Kaminska A, Lopez-Rosas A, Morfini G, Pigino G, Sands M, et al. (2013). The sphingolipid psychosine inhibits fast axonal transport in Krabbe disease by activation of GSK3b and deregulation of molecular motors. J. Neurosci 33, 10048–10056. [PubMed: 23761900]

Cantuti-Castelvetri L, Fitzner D, Bosch-Queralt M, Weil M-T, Su M, Sen P, Ruhwedel T, Mitkovski M, Trendelenburg G, Lütjohann D, et al. (2018). Defective cholesterol clearance limits remyelination in the aged central nervous system. Science 359, 684–688. [PubMed: 29301957]

Castelvetri LC, Givogri MI, Zhu H, Smith B, Lopez-Rosas A, Qiu X, van Breemen R, and Bongarzone ER (2011). Axonopathy is a compounding factor in the pathogenesis of Krabbe disease. Acta Neuropathol 122, 35–48. [PubMed: 21373782]

Clausen BE, Burkhardt C, Reith W, Renkawitz R, and Förster I (1999). Conditional gene targeting in macrophages and granulocytes using LysMcre mice. Transgenic Res 8, 265–277. [PubMed: 10621974]

Collier J, and Greenfield J (1924). The encephalitis periaxialis of Schilder. A clinical and pathological study, with an account of two cases, one of which was diagnosed during life. Brain 47, 489–519.

Coutinho MF, Prata MJ, and Alves S (2012). Mannose-6-phosphate pathway: a review on its role in lysosomal function and dysfunction. Mol. Genet. Metab 105, 542–550. [PubMed: 22266136]

Della-Flora Nunes G, Mueller L, Silvestri N, Patel MS, Wrabetz L, Feltri ML, and Poitelon Y (2017). Acetyl-CoA production from pyruvate is not necessary for preservation of myelin. Glia 65, 1626–1639. [PubMed: 28657129]

Dostert C, Pétrilli V, Van Bruggen R, Steele C, Mossman BT, and Tschopp J (2008). Innate immune activation through Nalp3 inflammasome sensing of asbestos and silica. Science 320, 674–677. [PubMed: 18403674]

Duchen LW, Eicher EM, Jacobs JM, Scaravilli F, and Teixeira F (1980). Hereditary leucodystrophy in the mouse: the new mutant twitcher. Brain 103, 695–710. [PubMed: 7417782]

Duewell P, Kono H, Rayner KJ, Sirois CM, Vladimer G, Bauernfeind FG, Abela GS, Franchi L, Nuñez G, Schnurr M, et al. (2010). NLRP3 inflammasomes are required for atherogenesis and activated by cholesterol crystals. Nature 464, 1357–1361. [PubMed: 20428172]

Escolar ML, Poe MD, Provenzale JM, Richards KC, Allison J, Wood S, Wenger DA, Pietryga D, Wall D, Champagne M, et al. (2005). Transplantation of umbilical-cord blood in babies with infantile Krabbe's disease. N. Engl. J. Med 352, 2069–2081. [PubMed: 15901860]

Ey B, Kobsar I, Blazyca H, Kroner A, and Martini R (2007). Visualization of degenerating axons in a dysmyelinating mouse mutant with axonal loss. Mol. Cell. Neurosci 35, 153–160. [PubMed: 17383197]

Feltri ML, D'antonio M, Previtali S, Fasolini M, Messing A, and Wrabetz L (1999). P0-Cre transgenic mice for inactivation of adhesion molecules in Schwann cells. Ann. N Y Acad. Sci 883, 116–123.

Galbiati F, Basso V, Cantuti L, Givogri MI, Lopez-Rosas A, Perez N, Vasu C, Cao H, van Breemen R, Mondino A, and Bongarzone ER (2007). Autonomic denervation of lymphoid organs leads to epigenetic immune atrophy in a mouse model of Krabbe disease. J. Neurosci 27, 13730–13738. [PubMed: 18077684]

Hagberg B, Kollberg H, Sourander P, andÅkesson HO (1969). Infantile globoid cell leucodystrophy (Krabbe's disease). A clinical and genetic study of 32 Swedish cases 1953–1967. Neuropadiatrie 1, 74–88. [PubMed: 5409293]

Hers HG (1965). Inborn lysosomal diseases. Gastroenterology 48, 625–633. [PubMed: 14280390]

Hoogerbrugge PM, Suzuki K, Suzuki K, Poorthuis BJ, Kobayashi T, Wagemaker G, and van Bekkum DW (1988). Donor-derived cells in the central nervous system of twitcher mice after bone marrow transplantation. Science 239, 1035–1038. [PubMed: 3278379]

Jacobs JM, Scaravilli F, and De Aranda FT (1982). The pathogenesis of globoid cell leucodystrophy in peripheral nerve of the mouse mutant twitcher. J. Neurol. Sci 55, 285–304. [PubMed: 7131035]

Kondo Y, Wenger DA, Gallo V, and Duncan ID (2005). Galactocerebrosidase-deficient oligodendrocytes maintain stable central myelin by exogenous replacement of the missing enzyme in mice. Proc. Natl. Acad. Sci. USA 102, 18670–18675. [PubMed: 16352725]

Kondo Y, Adams JM, Vanier MT, and Duncan ID (2011). Macrophages counteract demyelination in a mouse model of globoid cell leukodystrophy. J. Neurosci 31, 3610–3624. [PubMed: 21389217]

Krabbe K (1916). A new familial, infantile form of diffuse brain-sclerosis. Brain 39, 74–114.

Lappe-Siefke C, Goebbels S, Gravel M, Nicksch E, Lee J, Braun PE, Griffiths IR, and Nave K-A (2003). Disruption of Cnp1 uncouples oligodendroglial functions in axonal support and myelination. Nat. Genet 33, 366–374. [PubMed: 12590258]

Larocca JN, and Norton WT (2006). Isolation of myelin. Curr. Protoc. Cell Biol Published online January 2007. 10.1002/0471143030.cb0325s33.

Lee WC, Kang D, Causevic E, Herdt AR, Eckman EA, and Eckman CB (2010). Molecular characterization of mutations that cause globoid cell leukodystrophy and pharmacological rescue using small molecule chemical chaperones. J. Neurosci 30, 5489–5497. [PubMed: 20410102]

Li Y, Xu Y, Benitez BA, Nagree MS, Dearborn JT, Jiang X, Guzman MA, Woloszynek JC, Giaramita A, and Yip BK (2019). Genetic ablation of acid ceramidase in Krabbe disease confirms the psychosine hypothesis and identifies a new therapeutic target. Proc. Natl. Acad. Sci. USA 116, 20097–20103. [PubMed: 31527255]

Luddi A, Volterrani M, Strazza M, Smorlesi A, Rafi MA, Datto J, Wenger DA, and Costantino-Ceccarini E (2001). Retrovirus-mediated gene transfer and galactocerebrosidase uptake into twitcher glial cells results in appropriate localization and phenotype correction. Neurobiol. Dis 8, 600–610. [PubMed: 11493025]

MacDermot KD, Holmes A, and Miners AH (2001). Anderson-Fabry disease: clinical manifestations and impact of disease in a cohort of 60 obligate carrier females. J. Med. Genet 38, 769–775. [PubMed: 11732485]

Madisen L, Zwingman TA, Sunkin SM, Oh SW, Zariwala HA, Gu H, Ng LL, Palmiter RD, Hawrylycz MJ, Jones AR, et al. (2010). A robust and high-throughput Cre reporting and characterization system for the whole mouse brain. Nat. Neurosci 13, 133–140. [PubMed: 20023653]

Malone M (1970). Deficiency in a degradative enzyme system in globoid leukodystrophy. Trans. Am. Soc. Neurochem 1, 56.

Marshall MS, Issa Y, Jakubauskas B, Stoskute M, Elackattu V, Marshall JN, Bogue W, Nguyen D, Hauck Z, Rue E, et al. (2018). Long-term improvement of neurological signs and metabolic dysfunction in a mouse model of Krabbe's disease after global gene therapy. Mol. Ther 26, 874–889. [PubMed: 29433937]

Martini R, and Willison H (2016). Neuroinflammation in the peripheral nerve: Cause, modulator, or bystander in peripheral neuropathies? Glia 64, 475–486. [PubMed: 26250643]

Martino S, Tiribuzi R, Tortori A, Conti D, Visigalli I, Lattanzi A, Biffi A, Gritti A, and Orlacchio A (2009). Specific determination of β-galactocerebro sidase activity via competitive inhibition of β-galactosidase. Clin. Chem 55, 541–548. [PubMed: 19147730]

Martinon F, Pétrilli V, Mayor A, Tardivel A, and Tschopp J (2006). Gout-associated uric acid crystals activate the NALP3 inflammasome. Nature 440, 237–241. [PubMed: 16407889]

Matthes F, Andersson C, Stein A, Eistrup C, Fogh J, Gieselmann V, Wenger DA, and Matzner U (2015). Enzyme replacement therapy of a novel humanized mouse model of globoid cell leukodystrophy. Exp. Neurol 271, 36–45. [PubMed: 25956830]

Mikulka CR, and Sands MS (2016). Treatment for Krabbe's disease: Finding the combination. J. Neurosci. Res 94, 1126–1137. [PubMed: 27638598]

Miyatake T, and Suzuki K (1972). Globoid cell leukodystrophy: additional deficiency of psychosine galactosidase. Biochem. Biophys. Res. Commun 48, 539–543. [PubMed: 5047687]

Mosley K, and Cuzner ML (1996). Receptor-mediated phagocytosis of myelin by macrophages and microglia: effect of opsonization and receptor blocking agents. Neurochem. Res 21, 481–487. [PubMed: 8734442]

Nagano S, Yamada T, Shinnoh N, Furuya H, Taniwaki T, and Kira J (1998). Expression and processing of recombinant human galactosylceramidase. Clin. Chim. Acta 276, 53–61. [PubMed: 9760019]

Ono H, Ohta R, Kawasaki Y, Niwa A, Takada H, Nakahata T, Ohga S, and Saito MK (2018). Lysosomal membrane permeabilization causes secretion of IL-1β in human vascular smooth muscle cells. Inflamm. Res 67, 879–889. [PubMed: 30136196]

Peles E, Nativ M, Lustig M, Grumet M, Schilling J, Martinez R, Plowman GD, and Schlessinger J (1997). Identification of a novel contactin-associated transmembrane receptor with multiple domains implicated in protein-protein interactions. EMBO J 16, 978–988. [PubMed: 9118959]

Porrero C, Rubio-Garrido P, Avendaño C, and Clascá F (2010). Mapping of fluorescent protein-expressing neurons and axon pathways in adult and developing Thy1-eYFP-H transgenic mice. Brain Res 1345, 59–72. [PubMed: 20510892]

Rafi MA, Fugaro J, Amini S, Luzi P, de Gala G, Victoria T, Dubell C, Shahinfar M, and Wenger DA (1996). Retroviral vector-mediated transfer of the galactocerebrosidase (GALC) cDNA leads to overexpression and transfer of GALC activity to neighboring cells. Biochem. Mol. Med 58, 142–150. [PubMed: 8812733]

Rajamäki K, Lappalainen J, Oörni K, Välimäki E, Matikainen S, Kovanen PT, and Eklund KK (2010). Cholesterol crystals activate the NLRP3 inflammasome in human macrophages: a novel link between cholesterol metabolism and inflammation. PLoS ONE 5, e11765. [PubMed: 20668705]

Ramachandran P, Pellicoro A, Vernon MA, Boulter L, Aucott RL, Ali A, Hartland SN, Snowdon VK, Cappon A, Gordon-Walker TT, et al. (2012). Differential Ly-6C expression identifies the recruited macrophage phenotype, which orchestrates the regression of murine liver fibrosis. Proc. Natl. Acad. Sci. USA 109, E3186–E3195. [PubMed: 23100531]

Reddy AS, Kim JH, Hawkins-Salsbury JA, Macauley SL, Tracy ET, Vogler CA, Han X, Song S-K, Wozniak DF, Fowler SC, et al. (2011). Bone marrow transplantation augments the effect of brain- and spinal cord-directed adeno-associated virus 2/5 gene therapy by altering inflammation in the murine model of globoid-cell leukodystrophy. J. Neurosci 31, 9945–9957. [PubMed: 21734286]

Sands MS, and Davidson BL (2006). Gene therapy for lysosomal storage diseases. Mol. Ther 13, 839–849. [PubMed: 16545619]

Sawcer S, Hellenthal G, Pirinen M, Spencer CC, Patsopoulos NA, Moutsianas L, Dilthey A, Su Z, Freeman C, Hunt SE, et al.; International Multiple Sclerosis Genetics Consortium; Wellcome Trust Case Control Consortium 2 (2011). Genetic risk and a primary role for cell-mediated immune mechanisms in multiple sclerosis. Nature 476, 214–219. [PubMed: 21833088]

Schneider CA, Rasband WS, and Eliceiri KW (2012). NIH Image to ImageJ: 25 years of image analysis. Nat. Methods 9, 671–675. [PubMed: 22930834]

Schulz D, Severin Y, Zanotelli VRT, and Bodenmiller B (2019). In-depth characterization of monocyte-derived macrophages using a mass cytometry-based phagocytosis assay. Sci. Rep 9, 1925. [PubMed: 30760760]

Schwenk F, Baron U, and Rajewsky K (1995). A cre-transgenic mouse strain for the ubiquitous deletion of loxP-flanked gene segments including deletion in germ cells. Nucleic Acids Res 23, 5080–5081. [PubMed: 8559668]

Scott-Hewitt NJ, Folts CJ, Hogestyn JM, Piester G, Mayer-Pröschel M, and Noble MD (2017). Heterozygote galactocerebrosidase (GALC) mutants have reduced remyelination and impaired myelin debris clearance following demyelinating injury. Hum. Mol. Genet 26, 2825–2837. [PubMed: 28575206]

Seijffers R, Allchorne AJ, and Woolf CJ (2006). The transcription factor ATF-3 promotes neurite outgrowth. Mol. Cell. Neurosci 32, 143–154. [PubMed: 16713293]

Shin D, Feltri ML, and Wrabetz L (2016). Altered trafficking and processing of GALC mutants correlates with globoid cell leukodystrophy severity. J. Neurosci 36, 1858–1870. [PubMed: 26865610]

Sommer I, and Schachner M (1981). Monoclonal antibodies (O1 to O4) to oligodendrocyte cell surfaces: an immunocytological study in the central nervous system. Dev. Biol 83, 311–327. [PubMed: 6786942]

Spassieva S, and Bieberich E (2016). Lysosphingolipids and sphingolipidoses: Psychosine in Krabbe's disease. J. Neurosci. Res 94, 974–981. [PubMed: 27638582]

Suzuki K (1998). Twenty five years of the "psychosine hypothesis": a personal perspective of its history and present status. Neurochem. Res 23, 251–259. [PubMed: 9482237]

Suzuki K, and Grover WD (1970). Krabbe's leukocystrophy (globoid cell leukodystrophy). An ultrastructural study. Am. J. Obstet. Gynecol 106, 385–396. [PubMed: 5437261]

Suzuki K, and Suzuki Y (1970). Globoid cell leucodystrophy (Krabbe's disease): deficiency of galactocerebroside β-galactosidase. Proc. Natl. Acad. Sci. USA 66, 302–309. [PubMed: 5271165]

Svennerholm L, Vanier MT, and Månsson JE (1980). Krabbe disease: a galactosylsphingosine (psychosine) lipidosis. J. Lipid Res 21, 53–64. [PubMed: 7354254]

Swirski FK, Nahrendorf M, Etzrodt M, Wildgruber M, Cortez-Retamozo V, Panizzi P, Figueiredo J-L, Kohler RH, Chudnovskiy A, Waterman P, et al. (2009). Identification of splenic reservoir monocytes and their deployment to inflammatory sites. Science 325, 612–616. [PubMed: 19644120]

Trotter J, DeJong LJ, and Smith ME (1986). Opsonization with antimyelin antibody increases the uptake and intracellular metabolism of myelin in inflammatory macrophages. J. Neurochem 47, 779–789. [PubMed: 3734801]

Weinstock NI, Kreher C, Favret J, Bongarzone E, Wrabetz L, Feltri ML, and Shin D (2020). Brainstem development requires galactosylceramidase and is critical for the pathogenesis of Krabbe disease. bioRxiv 10.1101/2020.03.25.007542.

Weischenfeldt J, and Porse B (2008). Bone Marrow-Derived Macrophages (BMM): Isolation and Applications. CSH Protoc Published online December 1, 2008. 10.1101/pdb.prot5080.

Wilcox WR, Oliveira JP, Hopkin RJ, Ortiz A, Banikazemi M, Feldt-Rasmussen U, Sims K, Waldek S, Pastores GM, Lee P, et al.; Fabry Registry (2008). Females with Fabry disease frequently have major organ involvement: lessons from the Fabry Registry. Mol. Genet. Metab 93, 112–128. [PubMed: 18037317]

Wolf NI, Breur M, Plug B, Beerepoot S, Westerveld ASR, van Rappard DF, de Vries SI, Kole MHP, Vanderver A, van der Knaap MS, et al. (2020). Metachromatic leukodystrophy and transplantation: remyelination, no cross-correction. Ann. Clin. Transl. Neurol 7, 169–180. [PubMed: 31967741]

Wright MD, Poe MD, DeRenzo A, Haldal S, and Escolar ML (2017). Developmental outcomes of cord blood transplantation for Krabbe disease: A 15-year study. Neurology 89, 1365–1372. [PubMed: 28855403]

Yeager AM, Brennan S, Tiffany C, Moser HW, and Santos GW (1984). Prolonged survival and remyelination after hematopoietic cell transplantation in the twitcher mouse. Science 225, 1052–1054. [PubMed: 6382609]

Yunis EJ, and Lee RE (1970). Tubules of globoid leukodystrophy: a right-handed helix. Science 169, 64–66. [PubMed: 5463179]

Highlights

- Schwann cell Galc prevents psychosine-induced demyelination and neurodegeneration
- GALC transfer (cross-correction) is minimal in globoid cell leukodystrophy (GLD) cells
- Storage-laden macrophages (globoid cells) are direct mediators of GLD pathogenesis
- HSCT for GLD provides functional macrophages that are competent of phagocytosis

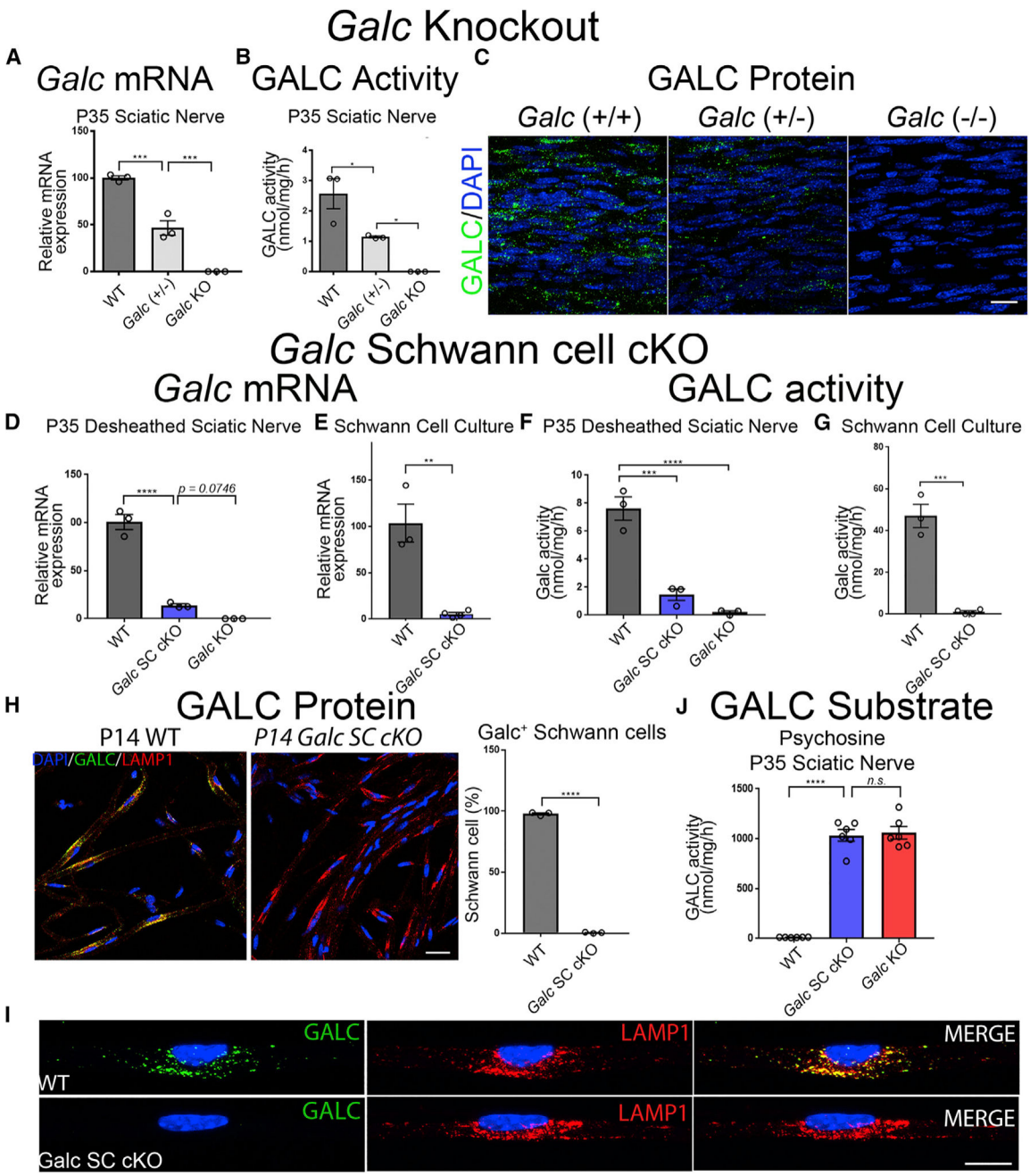

Figure 1. *Galc* Is Efficiently Ablated in Schwann Cells of Conditional Knockout Mice

(A–C) Dose-dependent reduction of GALC in P35 sciatic nerves from *Galc*$^{(+/+)}$, *Galc*$^{(+/-)}$, and *Galc*$^{(-/-)}$ mice.

(A) *Galc* mRNA expression, normalized to *β-Actin*, and reported relative to average WT expression.

(B) GALC enzymatic activity, measured as nmol of fluorogenic substrate MUGAL, normalized to protein and time.

(C) GALC immunofluorescence in longitudinal sections of P35 sciatic nerves. Polyclonal anti-GALC antibody (green); DAPI (blue).

(D–I) Efficient *Galc* ablation in Schwann cells of conditional knockout mice.
(D and E) *Galc* mRNA expression of desheathed P35 sciatic nerves (D) and primary Schwann cells (E).
(F and G) GALC activity of desheathed P35 sciatic nerves (F) and primary Schwann cells (G).
(H) GALC immunofluorescence and quantification of teased fibers from P14 sciatic nerves. GALC (green); LAMP1 (red); DAPI (blue). (I) Higher magnification of (H).
(J) Psychosine measured by HPLC-MS from P35 sciatic nerves.
Scale bars, 25 μm (C), 30 μm (H), and 14 μm (I). Error bars represent mean ± SEM, n = 3 biological replicates and 3 technical replicates per experiment (n = 6 for J). Statistical significance was calculated by one-way ANOVA (A, B, D, F, and J) or Student's t test (E, G, and H). In all figures, asterisks represent statistical significance (*p < 0.05, **p < 0.01; ***p < 0.005, ****p < 0.001). *n.s.*, not significant.

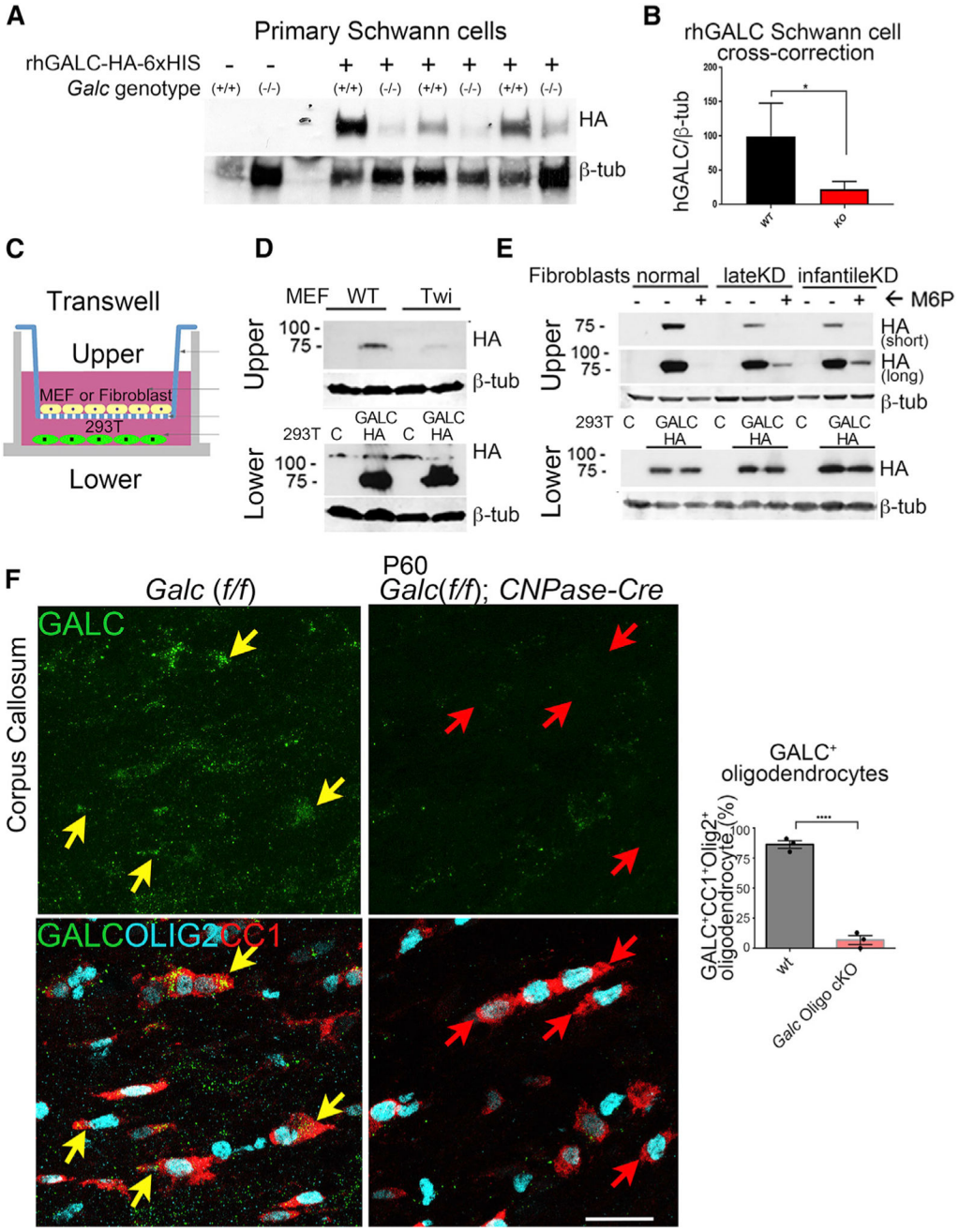

Figure 2. Cross-Correction Is Impaired in *Galc* Mutants

(A) Western blot of primary Schwann cells incubated with recombinant human GALC-HA-6xHis. Each lane represents a separate Schwann cell-culture preparation from a distinct animal. hGALC-HA bands were detected by western blot at the expected size of 80 kDa using an anti HA-HRP antibody.

(B) Quantification of rhGALC uptake from western blot in (A). Bands were quantified by densitometry for rhGALC and normalized to β-tubulin.

(C) Schematic of the transwell GALC uptake experiment for (D) and (E).

(D) Western blot of mouse embryonic fibroblasts in the top chambers or 293T cells in the lower chamber, after the transwell GALC-uptake assay.
(E) Control and GLD fibroblasts using the transwell GALC-uptake assay, as above. Infantile KD carried the homozygous 30 kb *GALC* deletion and late-onset KD had compound G286D/30 kb-del *GALC* mutations. 6 mM M6P was added where indicated.
(F) Immunofluorescence of corpus callosum white matter in WT and oligodendrocyte *Galc* cKO brains. The oligodendrocyte markers CC1 (red) and OLIG2 (cyan) co-localized with GALC (green) in WT brains, depicted by yellow arrows. Instead, KO brains had no GALC in CC1/OLIG2 double-positive oligodendrocytes (red arrows). Scale bar, 30 μm. Quantifications on right-hand side.
Error bars represent mean ± SEM, n = 3 biological replicates. For (B) and (F), a Student's t test was used to calculate statistical significance.

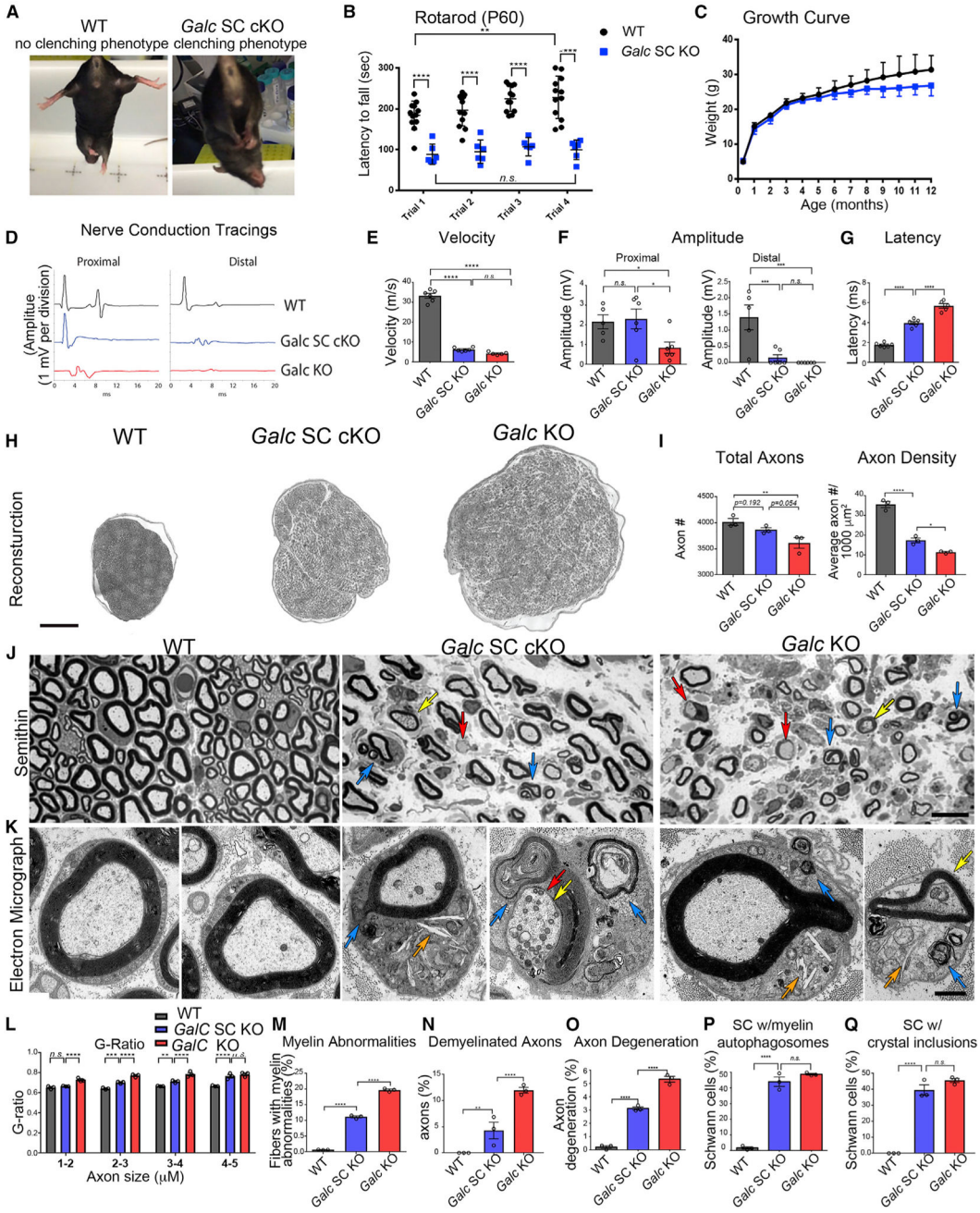

Figure 3. Ablation of Schwann Cell *Galc* Causes a Progressive Peripheral Neuropathy

(A) Clenching phenotype of P60 *Galc* SC cKO mice.

(B) Rotarod analysis of P60 mice. n = 6–12.

(C) Growth curve of mice. n = 6–12.

(D–G) Electrophysiology of sciatic nerves from P35 WT animals.

(D) Representative tracing from nerve conduction at proximal and distal sites.

(E) Nerve conduction velocities from P35 sciatic nerves.

(F) Proximal and distal amplitude from P35 sciatic nerves.

(G) Latency measurements from P35 sciatic nerves.

(H) Representative sciatic nerve reconstructions from P35 mice.
(I) Total axon count and myelinated axon density of whole P35 sciatic nerves (n = 3).
(J) Representative semithin sections of P35 sciatic nerves. Blue arrows indicate myelin abnormalities (outfoldings, infoldings, and degeneration), red arrows indicate demyelinated axons, and yellow arrows indicate axon degeneration.
(K) Representative electron micrographs of Schwann cells from P35 sciatic nerves. Blue arrows indicate degenerated myelin, orange arrows indicate crystals, yellow arrows indicate axon degeneration, and red arrows indicate demyelinated axons.
(L) G-ratio, as a function of axon size, from P35 sciatic nerves. n = 3 per genotype.
(M) Quantification of myelin abnormalities in P35 sciatic nerves.
(N) Quantification of demyelinated axons in P35 sciatic nerves.
(O) Quantification of degenerated axons in P35 sciatic nerves.
(P) Quantification of Schwann cells with accumulated myelin autophagosomes.
(Q) Quantification of Schwann cells with accumulated crystal inclusions.
Scale bars, 150 μm (H), 10 μm (J), and 1 μm (K). Error bars represent mean ± SEM, n = 3 biological replicates. Statistical significance was calculated by one-way ANOVA (E–G, I, and M–Q) or two-way ANOVA (B, C, and L).

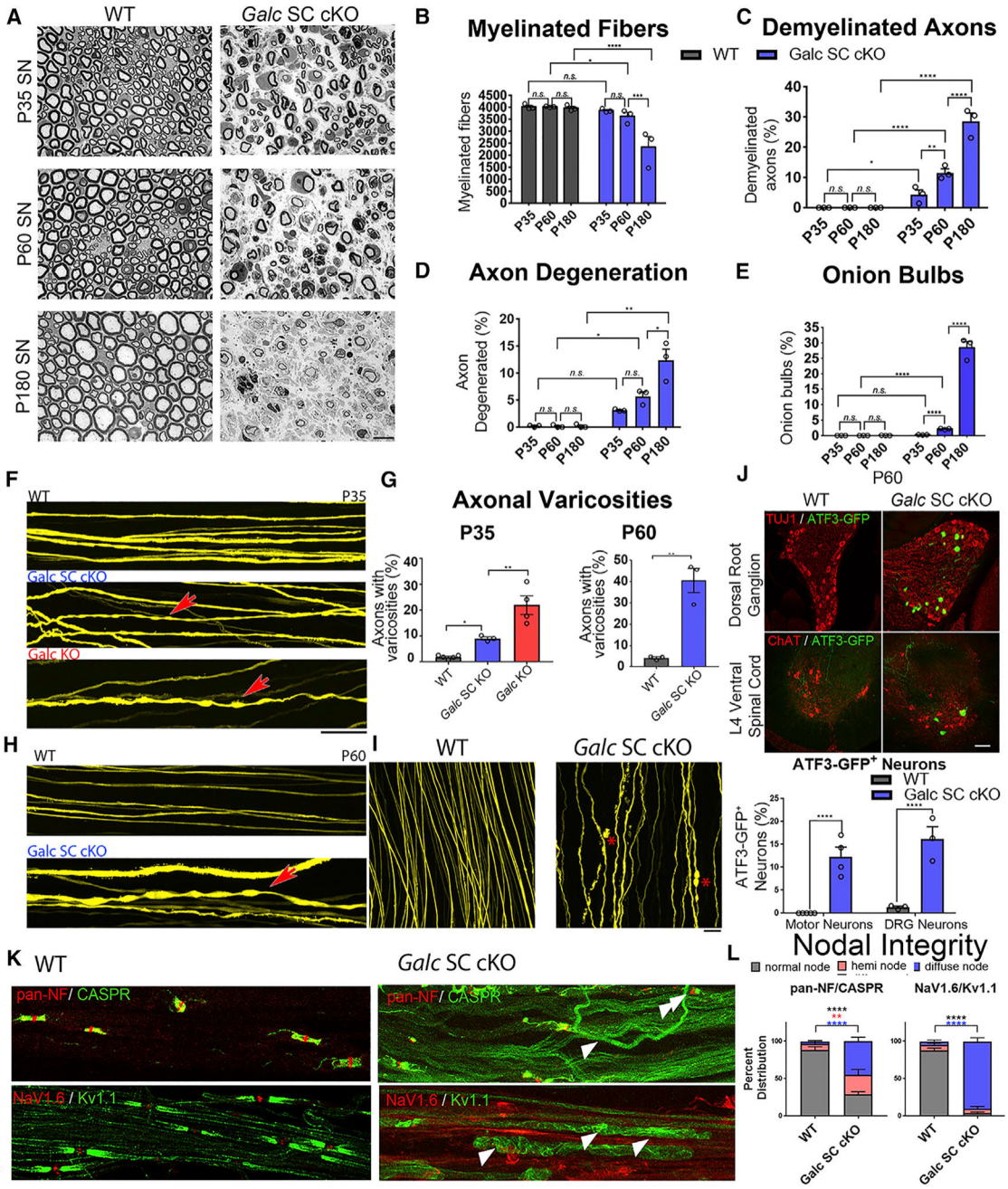

Figure 4. Deletion of *Galc* in Schwann Cells Causes a Progressive Demyelinating Neuropathy and Axonal Degeneration

(A) Semithin sections of sciatic nerve from P35, P60, and P180.

(B) Quantification of myelinated fibers in sciatic nerves of WT and *Galc* SC cKO at different ages.

(C) Percent of demyelinated axons in the sciatic nerves of WT and *Galc* SC cKO at different ages.

(D) Percent of degenerating axons in the sciatic nerves of WT and *Galc* SC cKO at different ages.

(E) Percent of fibers with onion bulbs in the sciatic nerves of WT and *Galc* SC cKO at different ages. (F) Thy1-YFP labelled axons of P35 sciatic nerve for the genotype indicated. Red arrow shows varicosities indicative of axonopathy.
(G) Quantification of varicosities (from F, left and H, right).
(H) Thy1-YFP labelled axons of P60 sciatic nerve in WT and *Galc* SC cKO nerves.
(I) P60 Thy1-YFP labelled axons showing examples of axon degeneration in *Galc* SC cKO, indicated by asterisk (red).
(J) ATF3-GFP expression and quantification in P60 DRG neurons or motor neurons.
(K) Evaluation of nodal integrity in sciatic nerve teased fibers stained with antibodies to the nodal and paranodal proteins Neurofascins (pan-NF, red); the paranodal protein Caspr (green), the nodal voltage-gated sodium channel NaV1.6 (red), and the juxtaparanodal potassium channel KV1.1 (green). Arrowheads point to fibers with abnormal diffuse localization of proteins, and double arrowheads point to heminodes.
(L) Quantification of (K).
Scale bars, 10 μm, 100 μm(F and H), and 40 μm(I). Error bars represent mean ± SEM, n = 3 biological replicates and 3 technical replicates per experiment (n = 4 for J). Statistical significance was calculated by two-way ANOVA (B–E), one-way ANOVA (P35, G), or Student's t test (P60 G, J, and L).

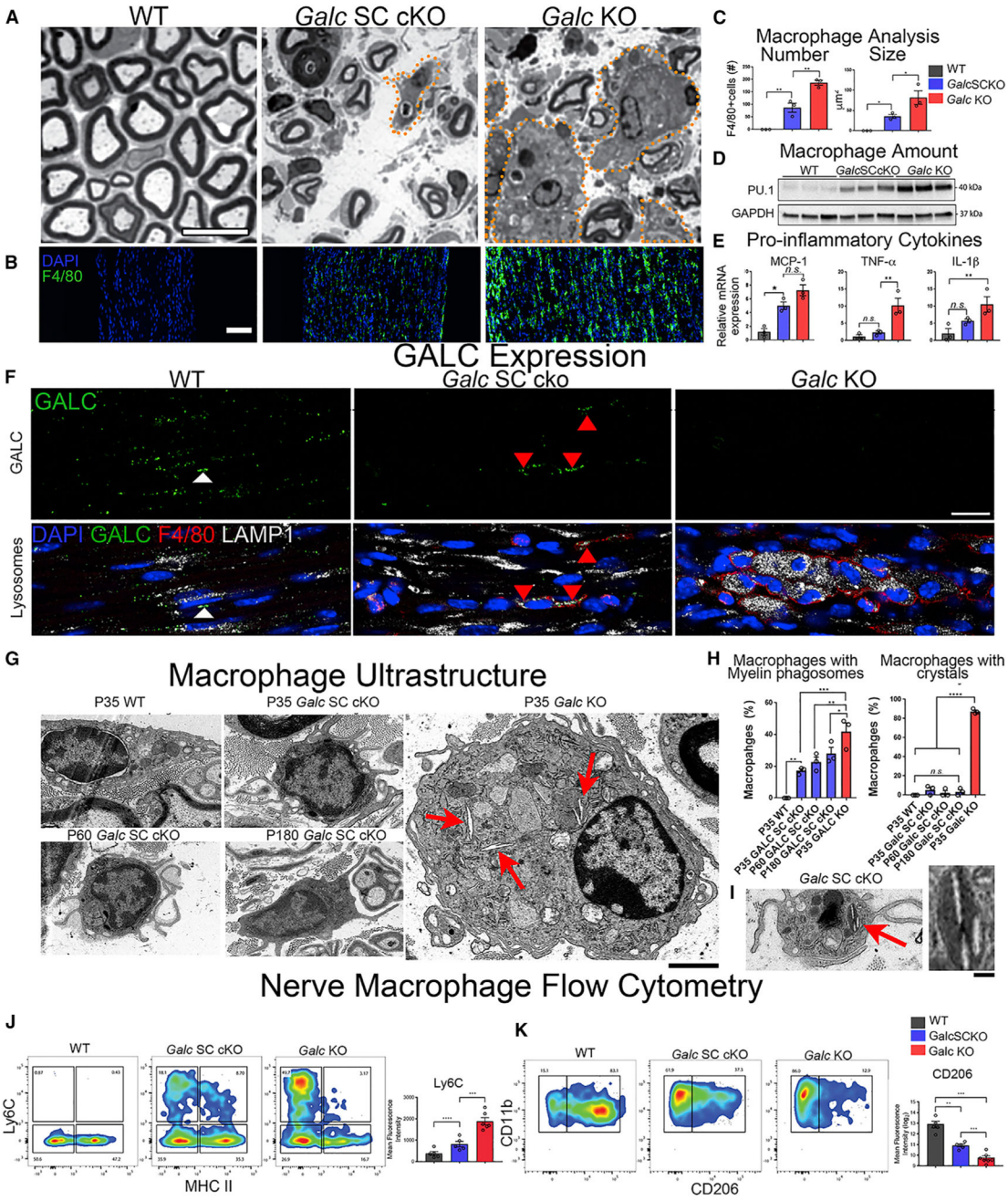

Figure 5. Macrophages Recruited to Sites of Demyelination Require GALC for Myelin Turnover

(A) Transverse semithin sections of P35 sciatic nerve (SN). Orange dotted lines outline macrophages.

(B) Immunofluorescence of macrophages in P35 sciatic nerve. Green, anti-F4/80; blue, DAPI.

(C) Quantification of macrophage number and size from (B).

(D) Western blot of macrophage marker PU.1 in P35 sciatic nerve.

(E) Quantitative RT-PCR of *Mcp-1*, *Tnf-α*, and *Il-1β* mRNA isolated from the sciatic nerve and normalized to *β-Actin*.

(F) Immunofluorescence of GALC expression in P35 nerves. Green, anti-GALC; red, anti-F4/80; blue, DAPI; white, anti-LAMP1. Scale bar, 30 μm.
(G) Electron microscopy (EM) of macrophages from sciatic nerves. Red arrows denote crystal inclusions. Scale bar, 2 μm.
(H) Quantifications of myelin phagosomes and crystals in macrophages from nerve.
(I) *Galc* SC cKO macrophage with crystal in EM. Inset is high magnification (scale bar, 200 nm).
(J) Representative plots of flow cytometry analysis of $CD11b^{+}/F4/80^{+}$ macrophages expressing MHC II and Ly6C from nerves (left) with quantification (right).
(K) Representative plots of flow cytometry analysis of $CD11b^{+}/F4/80^{+}$ macrophages expressing CD11b and CD206 from KO nerves (left) with quantification (right).
Scale bar, 10 μm (A), 50 μm (B), 30 μm (F), and 2 μm (G). Error bars represent mean ± SEM, n = 3–6 biological replicates and 3 technical replicates per experiment (n = 4 for J). One-way ANOVA was used to calculate statistical significance.

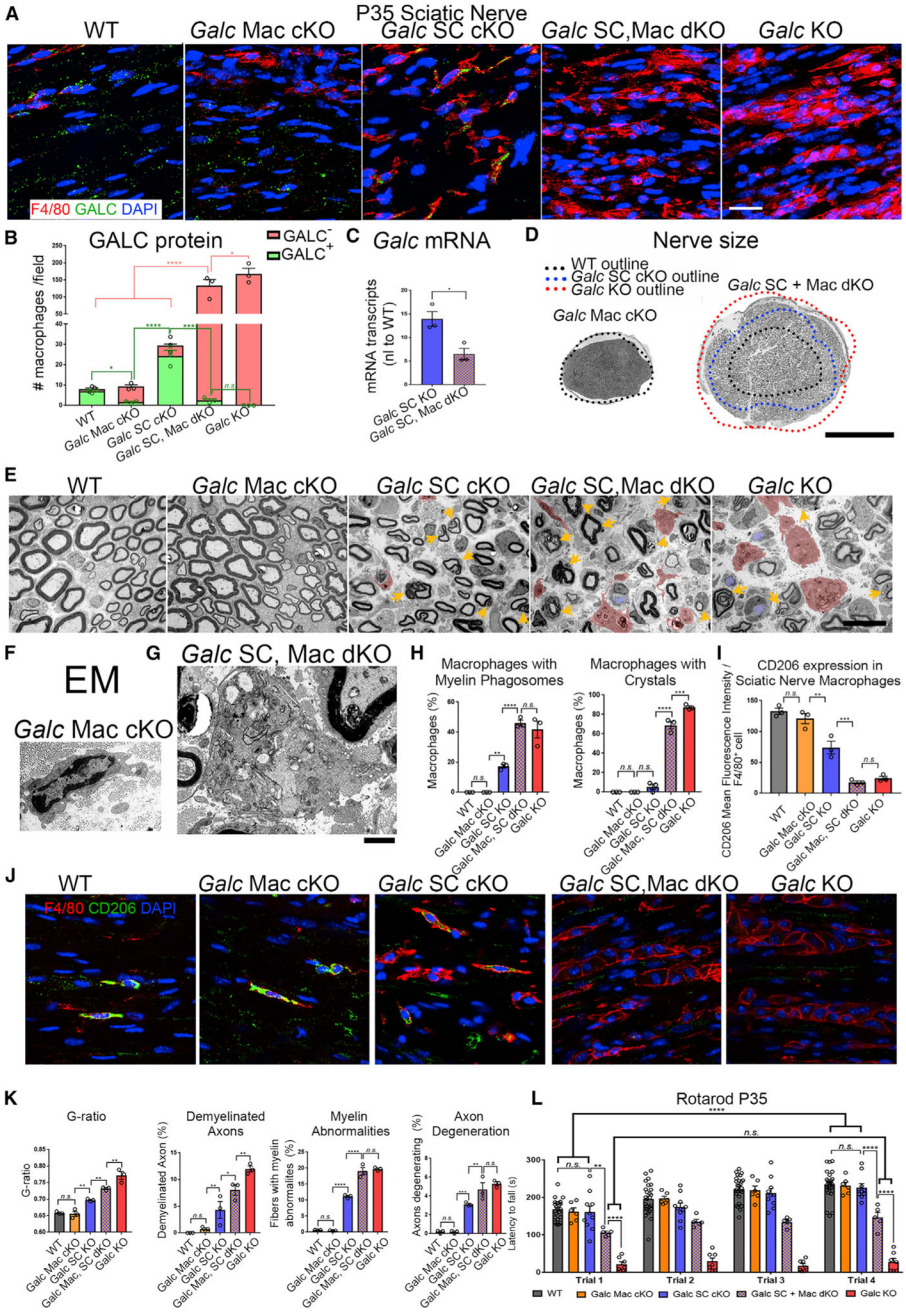

Figure 6. Concurrent Galc Ablation in Schwann Cells and Macrophages Recapitulates Peripheral GLD

(A) Immunofluorescence of macrophages (anti-F4/80; red) and GALC (green) in sciatic nerve longitudinal frozen sections.

(B) Quantification of GALC$^+$ and GALC$^-$ macrophages in P35 SN (from A). Pink and green bars represent the total number of GALC$^-$ and GALC$^+$ macrophages, respectively.

(C) Quantitative RT-PCR of *Galc* mRNA from P35 sciatic nerves. *Galc* normalized to β-*Actin* and reported relative to average WT expression.

(D) Reconstructions of P35 sciatic nerves. Black dotted line represents the outline of a WT sciatic nerve and matches the circumference of the *Galc* Mac cKO nerve diameter. Blue

dotted line represents the outline of a *Galc* SC cKO sciatic nerve. Red dotted line represents the outline of the full *Galc* KO nerve.

(E) EM of P35 SN shows macrophages pseudo-colored in red and demyelinated axons in blue. Yellow arrows reflect myelin abnormalities including degenerating myelin.

(F) EM of macrophage from P35 *Galc* Mac cKO sciatic nerves.

(G) EM of macrophage from P35 *Galc* SC, Mac dKO sciatic nerves.

(H) Quantification of macrophages with myelin phagosomes and crystals.

(I) Quantification of CD206 mean fluorescence intensity per F4/80 macrophage.

(J) Immunofluorescence of macrophages in P35 sciatic nerves with anti-CD206 (green), anti-F4/80 (red), and DAPI (blue).

(K) Quantification of average G-ratio and abnormalities shown in (E).

(L) Rotarod of P35 animals.

Scale bar, 25 μm (A), 300 μm (D), 10 μm (E), and 2 μm (F). Error bars represent mean ± SEM, n = 3 biological replicates and 3 technical replicates per experiment (n ≥ 6 for L). Statistical significance was calculated by one-way ANOVA (B, H, I, and K), Student's t test (C) or two-way ANOVA (L).

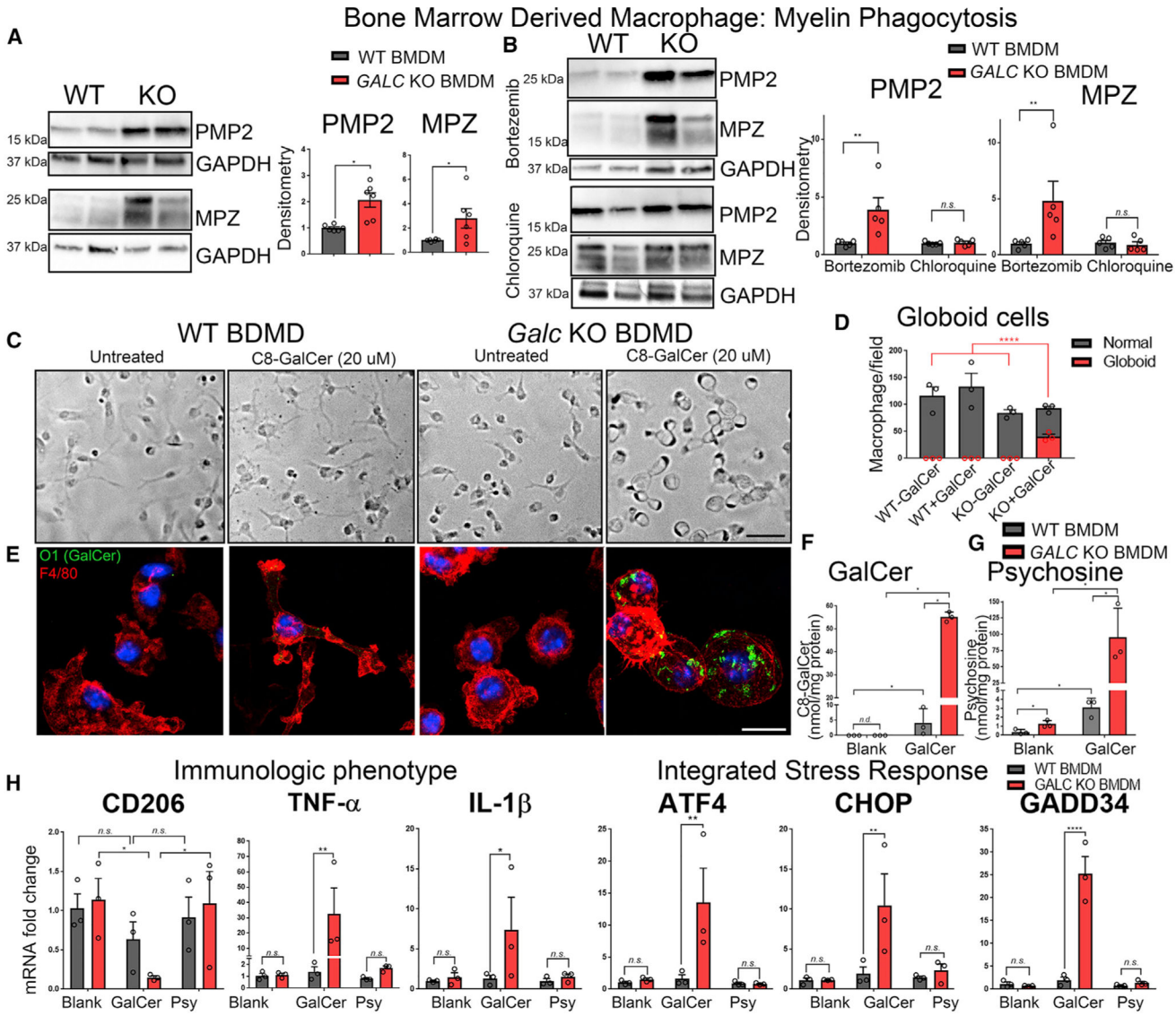

Figure 7. Galc-Deficient Macrophages Have a Defect in Myelin Degradation

(A) Western blot and quantification of Peripheral Myelin Protein 2 (PMP2) and Myelin Protein Zero (MPZ) after myelin phagocytosis assay.

(B) Western blot and quantification of PMP2 and MPZ when macrophages were co-incubated with myelin and either (i) the proteasome inhibitor bortezomib or (ii) the lysosome inhibitor chloroquine.

(C and D) Bright-field images (C) and quantification (D) of bone-marrow-derived macrophages in culture treated with either blank or C8-galactosylceramide for 24 h.

(E) Immunofluorescence of macrophages (anti-F4/80; red) cultured with C8-GalCer and stained for O1 (anti-GalCer; green) and DAPI (Blue).

(F and G) HPLC-MS measurement of C8-GalCer (F) and psychosine (G) from macrophages treated with 20 μM C8-GalCer.

(H) qPCR of BMDMs incubated with 20 μM DMSO (blank), 20 μM C8-GalCer, or 5 μM psychosine for markers related to the immunological phenotype and integrated stress response, normalized to β-*Actin*, and reported relative to average WT expression.
Scale bars, 60 μm (C) and 15 μm (E). Error bars represent mean ± SEM, n = 3 biological replicates and 3 technical replicates per experiment (n ≥ 5 for A and B). Statistical significance was calculated by Student's t test (A), one-way ANOVA (D), or two-way ANOVA (B, F, G, and H).

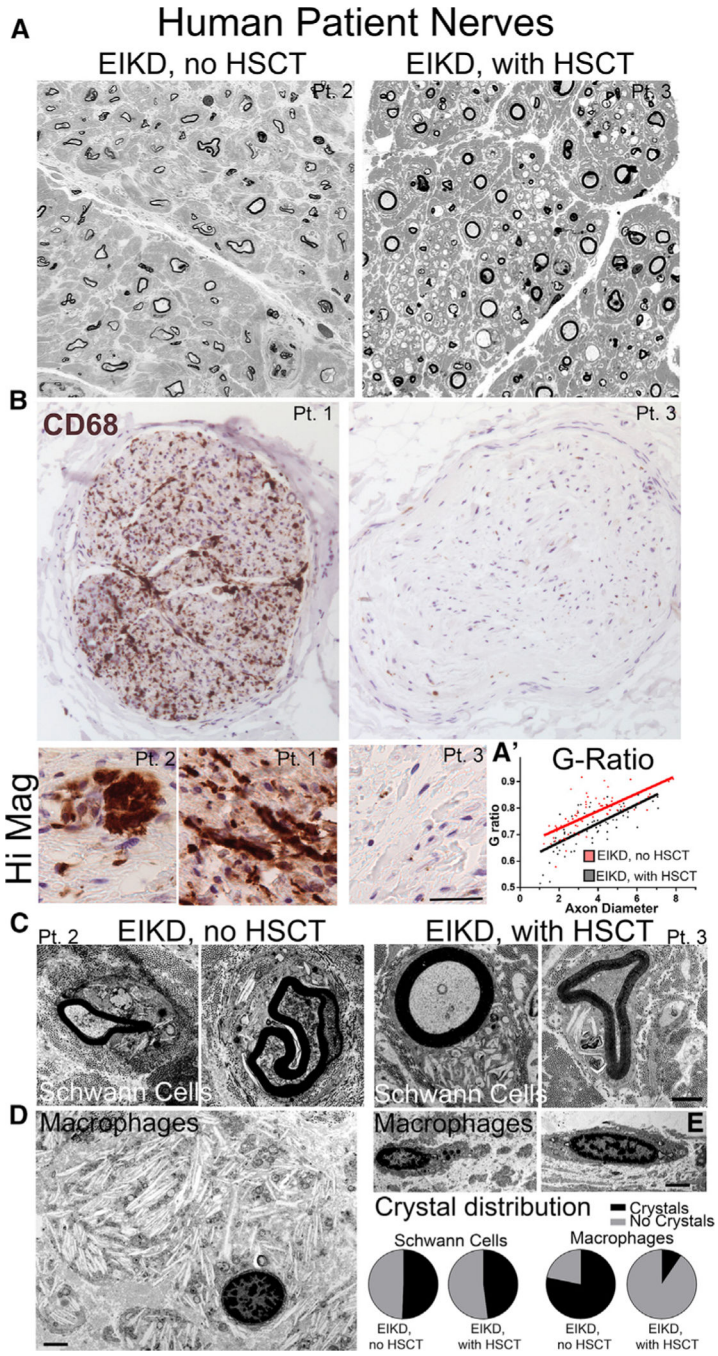

Figure 8. Macrophages Are Reduced and Have Normal Morphology in Nerves of EIKD Patients Who Received HSCT

(A) Semithin sections of brachial plexus nerves from EIKD patients who either did or did not receive HSCT show loss of fibers and thin myelin but is worse without HSCT treatment.

(B) CD68 IHC staining of femoral nerves from EIKD patients show abundant macrophages only in non-HSCT-treated patients

(C–E) Nerve EM show accumulation of crystals in Schwann cells from both patients (C) and in globoid cells from non-treated patients (D). Crystal deposits are significantly reduced and morphology is normal in macrophages from HSCT-treated patients (E).

Scale bar, 100 μm (B), 35 μm in high-magnification panels, and 2 μm (C–E).

KEY RESOURCES TABLE

REAGENT or RESOURCE	SOURCE	IDENTIFIER
Antibodies		
Rabbit anti-CASPR	A gift from Elior Peles, Weizmann Institute. (Peles et al., 1997)	#A6061 RRID:AB_231422 0
Mouse anti-APC (CC-1)	Millipore	Millipore Cat# OP80, RRID:AB_2057371
Mouse anti-CD-68	Dako (Agilent)	Agilent Cat# M0814, RRID:AB_2314148
Rabbit anti-CD206	Proteintech	Cat# 18704–1-AP RRID:AB_105972 32
Goat anti-Choline Acetyltransferase (ChAT)	Millipore	Millipore Cat# AB144P, RRID:AB_2079751
Rat anti-mouse F4/80	Bio-Rad	Bio-Rad Cat# MCA497GA, RRID:AB_323806
Chicken anti-GALC	A gift from Chris Lee and Christopher Eckman. (Lee et al., 2010)	CL1021AP
Rabbit anti-GAPDH	Sigma-Aldrich	Sigma-Aldrich Cat# G9545, RRID:AB_796208
Rat anti-HA High Affinity	Roche	Roche Cat# 11867423001, RRID:AB_390918
Anti-HA-Peroxidase, High Affinity	Roche	Roche Cat# 12013819001, RRID:AB_390917
Rabbit anti-IBA1 (for immunocytochemistry)	Wako Chemicals	Cat# 019–19741 RRID:AB_839504
Rabbit anti-Kv1.1 (KCNA1)	Alomone Labs	Cat# APC-009, RRID:AB_204014 4
Rabbit anti-LAMP-1	Abeam	Abcam Cat# ab24170, RRID:AB_775978
Chicken anti-MPZ	Aves	Aves Labs Cat# PZO, RRID:AB_2313561
Rabbit anti-MPZ	Abeam	Abcam Cat# ab31851, RRID:AB_2144668
Mouse anti-Nav1.6 clone K87A/10	UC Davis / NeuroMab	RRID:MMRRC_06 5966-UCD
Mouse anti-Pan-Neurofascin L11A/41	Millipore	Millipore Cat# MABN621 RRID: AB_10672370
Anti-galactocerebroside (O1)	A gift from Pablo Paez, SUNY Buffalo. (Sommer and Schachner, 1981)	O1 Hybridoma
Rabbit anti-human OLIG2	Proteintech	Proteintech Cat# 13999–1-AP, RRID:AB_2157541
Rabbit anti-PMP2	Proteintech	Proteintech Cat# 12717–1-AP, RRID:AB_2166978
Rabbit anti-PU.1 (Spi-1) (T-21)	Santa Cruz	Santa Cruz Biotechnology Cat# sc-352, RRID:AB_632289
Mouse anti-Tubulin β3 (Tuj1)	Biolegend	Covance Cat# MMS-435P, RRID:AB_2313773
Rabbit anti-β-Tubulin	Novus	Novus Cat# NB600–936, RRID:AB_1000065 6
Brilliant Violet 711 anti-mouse/human CD11b antibody (M1/70)	BioLegend	Cat# 101241 RRID:AB_112187 91
PE anti-mouse Ly-6G antibody (1A8)	BioLegend	Cat# 127607 RRID:AB_118610 4
APC anti-mouse F4/80 antibody (BM8)	BioLegend	Cat# 123115 RRID:AB_ 893493
PE/Cy7 anti-mouse Ly-6C antibody (HK1.4)	BioLegend	Cat# 128017 RRID:AB_ 1732093
FITC Hamster Anti-Mouse CD11C (HL3)	BD PharMingen	Cat# 553801 RRID:AB_395060
APC/Cy7 anti-mouse CD86 antibody (GL-1)	BioLegend	Cat# 105029 RRID: AB_2074993

REAGENT or RESOURCE	SOURCE	IDENTIFIER
PerCP anti-mouse I-A/I-E antibody (M5/114.15.2)	BioLegend	Cat# 107623 RRID: AB_893586
Brilliant Violet 510 anti-mouse/human CD11b antibody (M1/70)	BioLegend	Cat# 101245 RRID:AB_256139 0
APC/Cyanine7 anti-mouse F4/80 antibody (BM8)	BioLegend	Cat# 123117 RRID: 893489
iNOS Monoclonal antibody (CXNFT), APC, eBioscience	Thermo Fisher Scientific	Cat#17-5920-82 RRID:AB_257324 4
Human/Mouse Arginase 1/ARG1 Fluorescein- conjugated antibody	R&D Systems	Cat#IC5868F RRID:AB_107181 18
PE/Cy7 anti-mouse CD206 (MMR) antibody (C068C2)	BioLegend	Cat# 141719 RRID:AB_256224 7
EGR2 Monoclonal Antibody (erongr2), PE, eBioscience	Thermo Fisher Scientific	Cat# 12-6691-82 RRID:AB_107178 04
Brilliant Violet 711 anti-mouse TNF-α antibody (MP6-XT22)	BioLegend	Cat# 506349 RRID:AB_262980 0
Brilliant Violet 421 anti-human IL-10 antibody (JES3–9D7)	BioLegend	Cat# 501421 RRID:AB_108969 47
PerCP/Cy5.5 anti-mouse IL-12/IL-23 p40 (monomer, dimer, heterodimer) antibody (C15.6)	BioLegend	Cat# 505211 RRID:AB_256622 4
TruStain FcX (anti-mouse CD16/32) antibody (93)	BioLegend	Cat#101319 RRID:AB_157497 3
Alexa Fluor 488-AffiniPure F(ab')2 Fragment Donkey anti-Chicken IgY	Jackson ImmunoResearch Labs	Jackson ImmunoResearch Labs Cat# 703-546-155, RRID:AB_2340376
Rhodamine Red-X-AffiniPure Donkey Anti-Rabbit IgG	Jackson ImmunoResearch Labs	Jackson ImmunoResearch Labs Cat# 711-295-152, RRID:AB_2340613
Alexa Fluor 647 AffiniPure F(ab')$_2$ Fragment Donkey Anti-Rabbit IgG	Jackson ImmunoResearch Labs	Jackson ImmunoResearch Labs Cat# 711-606-152, RRID:AB_2340625
Goat anti-Mouse lgG2b Cross-Adsorbed Secondary Antibody, Alexa Fluor 594	Thermo Fisher Scientific	Thermo Fisher Scientific Cat# A- 21145, RRID:AB_2535781
Alexa Fluor 594-AffiniPure Goat Anti-Mouse IgG, Fc subclass 2a Specific antibody	Jackson ImmunoResearch Labs	Jackson ImmunoResearch Labs Cat# 115-585-206, RRID:AB_2338886
Cy3-AffiniPure Donkey Anti-Goat IgG (H+L) antibody	Jackson ImmunoResearch Labs	Jackson ImmunoResearch Labs Cat# 705-165-003, RRID:AB_2340411
Alexa Fluor 488-AffiniPure Donkey Anti-Rat IgG antibody	Jackson ImmunoResearch Labs	Jackson ImmunoResearch Labs Cat# 712-545-153, RRID:AB_2340684
Rhodamine (TRITC)-AffiniPure Donkey Anti-Rat IgG antibody	Jackson ImmunoResearch Labs	Jackson ImmunoResearch Labs Cat# 712-025-153, RRID:AB_2340636
Donkey Anti-Rabbit Rabbit IgG (H+L) Polyclonal, HRP-Conjugated antibody	Novus	Novus Cat# NB 7185, RRID:AB_524677
Peroxidase-AffiniPure Donkey Anti-Chicken IgY (IgG) antibody	Jackson ImmunoResearch Labs	Jackson ImmunoResearch Labs Cat# 703-035-155, RRID:AB_1001528 3
Peroxidase-AffiniPure Goat Anti-Rat IgG, Light Chain Specific	Jackson ImmunoResearch Labs	Jackson ImmunoResearch Labs Cat# 112-035-175, RRID:AB_2338140
Goat anti-Mouse IgM, mu chain, FITC conjugate antibody, Millipore	Millipore	Millipore Cat# AP128F, RRID:AB_1121579 1
Bacterial and Virus Strains		
DH5a	Thermo Fisher Scientific	Catalog number: 1825801 2
Biological Samples		
Mouse Nerve RNA	This paper	N/A
Mouse Schwann cell RNA	This paper	N/A
Mouse BMDM RNA	This paper	N/A
Chemicals, Peptides, and Recombinant Proteins		
2,2,2-tribromoethanol (avertin)	Millipore Sigma	Cat#T48402
4-methylumbelliferone β-D-galactopyranoside	Sigma-Aldrich	Cat#M1633

REAGENT or RESOURCE	SOURCE	IDENTIFIER
4-methylumbelliferone sodium salt	Sigma-Aldrich	Cat#M1508
Amicon Ultra-15	Fisher Scientific	Cat#UFC901024
C8 galactosyl ceramide	Avanti Polar Lipids	Cat#860538P
Diethyl pyrocarbonate (DEPC)	Fisher Scientific	Cat#FERR0601
D-Mannose 6-phosphate	Sigma-Aldrich	Cat#M6876
DNA 100bp ladder	Goldbiotechnology	Cat#D001–2500
Pierce ECL Western Blotting	Thermo Fisher Scientific	Cat#32106
Pierce ECL Plus Western Blotting	Thermo Fisher Scientific	Cat#32132
GE Healthcare Amersham	Fisher Scientific	Cat#45-001-507PM
HisPur Cobalt Resin	Thermo Fisher Scientific	Cat#89964
Imidazole	Millipore Sigma	Cat#T6330
β-Mercaptoethanol	Sigma-Aldrich	Cat#M6250
Phosphatase Cocktail 2	Sigma-Aldrich	Cat#P5726
Phosphatase Cocktail 3	Sigma-Aldrich	Cat#P0044
PMSF	Sigma-Aldrich	Cat#45-P7626
Precision Plus Protein Dual Color Standards	Bio-Rad	Cat#161–0394
Psychosine (Galactosyl Sphingosine, d18:1)	Avanti Polar Lipids	Cat#860537P
Deuterated Psychosine Quantitative Mass Spec Standard	Avanti Polar Lipids	Cat#330714W
Saponin	Sigma-Aldrich	Cat#47036
Thermo Scientific Pierce Tissue Strainers (250 microns)	Fisher Scientific	Cat#87791
Vectashield Antifade Mounting Medium	Vector Labs	Cat#H-1000
Vetabond reagent for tissue section (TESPA)	Vector Labs	Cat#SP-1800
B27 Supplement	Thermo Fisher Scientific	Cat#17504–044
Collagen	Corning	Cat#354236
Collagenase type I	Fischer Scientific	Cat#NC9633623
Dispase II	Sigma-Aldrich	Cat#D4693
Forskolin	EMD Millipore	Cat#344270
Human Recombinant Laminin 211	Biolamina	Cat#LN211–03
Lipofectamine 3000	Thermo Fisher Scientific	Cat#L3000008
Recombinant Human Nrg1-β1	R&D Systems	Cat#396-HB-050
Recombinant Mouse M-CSF	Biolegend	Cat#576404
RPMI-1640 medium	Thermo Fisher Scientific	Cat#21870076
Nerve Growth Factor NGF	Envigo	Cat#BT.5017
Opti-MEM	Thermo Fisher Scientific	Cat#11058–021
Critical Commercial Assays		
Cell counting kit-8	Dojindo	Cat#CK04–05
Cholesterol Assay Kit (aka Filipin)	Abeam	Cat#Ab133116
Fixation/Permeabilization Solution Kit	BD Cytofix/Cytoperm	Cat#554714
Reverse Transcriptase (superscript III Kit)	Thermo Fisher Scientific	Cat#18080–051
Taqman Gene Expression Assay: 18S (Hs99999901_s1)	Thermo Fisher Scientific	Cat#4331182
Taqman Gene Expression Assay: Ddit3/CHOP (Mm00492097_m1)	Thermo Fisher Scientific	Cat#4331182

REAGENT or RESOURCE	SOURCE	IDENTIFIER
Taqman Gene Expression Assay: XBP1 (Mm03464496_m1)	Thermo Fisher Scientific	Cat#4331182
Taqman Gene Expression Assay: HSPa5/BiP (Hs99999174_m1)	Thermo Fisher Scientific	Cat#4331182
Taqman Gene Expression Assay: MRC1/CD206 (Mm01329362_m1)	Thermo Fisher Scientific	Cat#4331182
Experimental Models: Cell Lines		
Human: Dermal Fibroblasts	Telethon biobank (Shin et al., 2016)	N/A
Mouse: Primary Schwann cells	This paper	N/A
Mouse: Primary bone marrow derived macrophages	This paper	N/A
Mouse: Primary embryonic fibroblasts	This paper	N/A
Experimental Models: Organisms/Strains		
Mouse: B6.C-Tg(GALC$^{fl/fl}$)	This paper. (Weinstock et al., 2020)	N/A
Mouse: B6.CE-Galc^{twi}/J	The Jackson Laboratory	Cat#000845
Mouse: B6.C-Tg(CMV-cre)1Cgn/J	The Jackson Laboratory	Cat#006054
Mouse: B6N.FVB-Tg(Mpz-cre)26Mes/J (aka PO Cre)	The Jackson Laboratory	Cat#017927
Mouse: B6.129P2-Lyz2$^{tm1(cre)Ifo}$/J (aka LysM Cre)	The Jackson Laboratory	Cat#004781
Mouse: B6;129S6-Gt(ROSA)26Sor$^{tm14(CAG-dTomato)Hze}$/J (aka tdTomato)	The Jackson Laboratory	Cat#007908
Mouse: B6.Cg-Tg(Thy1-YFP)HJrs/J	The Jackson Laboratory	Cat# 003782
Mouse: ATF3-GFP	Y.-C.C. and C. Woolf unpublished data	N/A
Oligonucleotides		
Primers for qPCR, See Table S2	This paper	N/A
Primers for cloning hGALC-6xHis-HA, see Table S2	This paper	N/A
Recombinant DNA		
hGALC-HA	(Shin et al., 2016))	N/A
hGALC-6xHis-HA	This paper	N/A
Software and Algorithms		
ImageJ	(Schneider et al., 2012)	https://imagej.net/Welcome
Graph Pad Prism 7	GraphPad	Graphpad.com